

Implications of Sea Breeze Circulations on Boundary Layer Aerosols in the Southern Coastal Texas Region

Tamanna Subba¹, Michael P. Jensen¹, Min Deng¹, Scott E. Giangrande¹, Mark C. Harvey², Ashish Singh¹, Die Wang^{1,3}, Maria Zawadowicz¹, Chongai Kuang¹

¹Environmental Science and Technologies, Brookhaven National Laboratory, Upton, NY, United States

²Department of Physics, Texas Southern University, Houston, TX, United States

³Institute for Atmospheric and Climate Science, ETH Zürich, Universitätstrasse 16, Zürich 8092, Switzerland

Correspondence: Tamanna Subba (tsubba@bnl.gov)

Abstract

The Sea Breeze Circulation (SBC) influences atmospheric processes at multiple scales in coastal regions. Understanding how SBCs impact the aerosol number budget and aerosol-cloud interaction processes is essential. This study investigates sea breeze–aerosol interactions (SAIs) during 46 summertime SBC events using data from the TRacking Aerosol Convection Interactions Experiment (TRACER) field campaign across urban (main) and rural (supplemental) coastal sites in southern Texas. Weather Research and Forecasting model coupled with Chemistry (WRF-Chem) simulations complement observations to explore spatio-temporal meteorological controls on boundary layer aerosols. During the summertime, Sea Breeze Fronts (SBF) penetrating inland transported cool, moist air over the land, introducing air masses with distinct properties compared to the preexisting continental air. These SAIs cause variability in number concentrations of up to a factor of two, with events typically lasting ~5 hours before returning to background conditions. SAI impact on aerosols varies with site proximity to water and the preceding sea breeze (SB) history, primarily affecting the marine-influenced accumulation mode. The main site, influenced by both Galveston Bay and the Gulf of Mexico, reflects a stronger marine influence. In contrast, a supplemental site, at a similar shoreline distance but exposed only to the Gulf of Mexico and typically upstream of the urban core, samples SB air that has traversed land and partially regained continental characteristics. Simulations show that the regional SAIs extend ~50 km inland and reach up to the boundary

31 layer height. SAIs further decrease cloud condensation nuclei relevant aerosol number
32 concentrations in ~20% of events during SBF passage.

33 **1 Introduction**

34 A significant portion of the global population resides in coastal cities, including several
35 megacities (Brown et al., 2013). Nearly half of the U.S. population faces environmental
36 challenges associated with complexities tied to urban coastal atmospheres (Crossett et al.,
37 2004; Hudson et al., 2012). Houston, located along the Southern Texas coastline, is one of the
38 United States' most populated cities, while also one of its most polluted, with high aerosol
39 concentrations (Yoon et al., 1994; Kleinman et al., 2002; Banta et al., 2011). Aerosol particles
40 can negatively impact human health (Partanen et al 2018; Mack et al., 2020), and influence
41 Earth's energy balance. They exert direct effects by scattering and absorbing the incoming solar
42 radiation, altering net radiative fluxes (Charlson et al., 1992; Bond et al., 2013; IPCC, 2021),
43 and indirect effects by acting as cloud condensation nuclei (CCN) and ice nucleating particles
44 (INP), thereby modulating cloud microphysical properties and precipitation processes
45 (Twomey, 1974; Albrecht et al., 1989; Ramanathan et al., 2001; Rosenfeld et al., 2008; Ariya
46 et al., 2009; Burkart et al., 2021).

47 In particular, the Houston region experiences highly complex aerosol processes due to
48 elevated local emissions, diverse aerosol sources, and intricate atmospheric chemistry. One
49 such process is new particle formation (NPF), which is a common aerosol microphysical
50 process that impacts the overall aerosol number concentration (Kulmala et al., 2004; Kerminen
51 et al., 2005; Kuang et al., 2008; IPCC 2013). NPF events typically include a sudden burst of
52 aerosols, i.e., the nucleation of gas molecules and formation of stable clusters of diameters
53 ' D_p ' > 2 nm, followed by subsequent growth, firstly to a size range with D_p > 50 nm and
54 possibly growing to a size where the particles can act as a CCN (D_p > 100 nm) (Yu and Luo,
55 2009; Kerminen et al., 2012; Gordon et al., 2017). In addition, mesoscale meteorological
56 phenomenon around Houston, such as sea breeze circulations (SBCs), further modulate these
57 aerosol dynamics (e.g., Miller et al., 2003; Wang et al., 2024; Deng et al., 2025; Thompson et
58 al., 2025). These SBCs develop regularly in the warm season along coastal regions (Miller et
59 al., 2003). One key challenge for aerosol process studies common to coastal city environments
60 is in determining the relative importance of aerosol microphysical versus mesoscale
61 meteorological controls such as SBCs, in governing the aerosol number budget and aerosol
62 impacts on that population center.

63 The summertime SBC is a thermally-driven feature tied to differential heating between
64 the land and sea; this results in density gradients that cause the cooler marine air to propagate
65 inland (Miller et al., 2003; di Bernardino et al., 2021). Daytime SBC formation can facilitate
66 convective cloud and precipitation onset (Comin et al., 2015), influence boundary layer
67 meteorology (Adaricheva et al., 2023), and has been associated with complex impacts on
68 overall air quality (Simpson, 1994; Masselink and Pattiaratchi, 1998; Moorthy et al., 2003;
69 Miller et al., 2003; Augustin, et al., 2020; Park et al., 2020; Parajuli et al., 2022; Wang et al.,
70 2023). These circulations also influence transport of atmospheric gases (Gangoiti et al., 2001;
71 Ahmadov et al., 2007; Hernández-Ceballos et al., 2015) and aerosol particles (Clappier et al.,
72 1999; Borge et al., 2008; Papanastasiou et al., 2010). A sea breeze front (SBF), which is the
73 boundary between that cooler, more moist marine air of the SBC flow and the warmer, drier
74 air over the land, is often a focal point that facilitates the transport and dispersal of aerosols, as
75 well as aiding in the formation of cumulus clouds (Miller et al., 2003). While low-level lapse
76 rates are often more stable on the maritime side of the SBF, the conditional instability
77 (Convective Available Potential Energy-CAPE) is often observed to be greater on the maritime
78 side due to the higher moisture content in that air mass (Hanft and Houston, 2018; Sharma et
79 al., 2024; Boyer et al., 2025). Convergence along these SBFs often results in enhanced upward
80 air motion, allowing aerosols to ascend to higher altitudes ~2 km (Iwai et al., 2011). Stronger
81 wind shear along these SBFs also generates increased turbulence, as owing to Kelvin-
82 Helmholtz instability occurring just behind this front (Linden and Simpson, 1986; Plant and
83 Keith, 2007), while the aforementioned vertical air motions are important for convective cloud
84 initiation (Rao and Fuelberg, 2000; Arrillaga et al., 2020).

85 The common conceptual model for SBCs is one where the marine air mass propagates
86 inland, bringing with it different atmospheric and aerosol characteristics compared to the
87 ambient land air mass conditions. In this study, the influence of these SBCs on regional aerosols
88 is termed as “sea breeze - aerosol interaction” (SAI). Previous studies have shown that SAIs
89 vary depending on complex interactions among emissions sources, boundary layer dynamics,
90 and the strength and/or direction of the SBC (Miller et al., 2003; Boyouk et al., 2011; di
91 Bernardino et al., 2021). For example, SBF passage has been found to trap aerosols at lower
92 elevations within the boundary layer (Miller et al., 2003). In SBC environments, competing
93 processes can yield opposite aerosol responses, as the formation of a shallow thermal boundary
94 layer can confine particles near the surface and raise aerosol concentrations, whereas inland

95 buoyant (convective) lifting within the convective boundary layer, can lift aerosols aloft
96 (Simpson, 1994; Boyouk et al., 2011; di Bernardino et al., 2021). In addition, SBCs may
97 replace the regional air mass with the cleaner marine air mass, leading to a decrease in surface
98 aerosol concentration. This now-modified coastal environment can affect the generation and
99 growth of aerosols, impacting the local aerosol number budget that further influences their
100 direct and indirect effects.

101 Although several studies have investigated the overall change in the aerosol loading
102 during SBC events, less is known about the role of SAI on the aerosol microphysical properties.
103 Moorthy et al. (1993) observed that the passage of the SBF was associated with an increase in
104 the concentration of smaller particles. Furthermore, since SBFs propagate inland, SBCs can
105 have far-reaching impacts on aerosol properties (Iwai et al., 2011; Park and van den Heever,
106 2022). As an example, previous studies conducted in the Southeastern United States indicated
107 that inland propagating SBFs are followed by air masses that often contrasted with regional air,
108 having potential influence on distances 220 km from the Gulf of Mexico (Viner et al., 2021;
109 Bao et al., 2023). In a similar case of these farther-reaching influences, Parajuli et al. (2020)
110 found that the SBC influences the aerosol vertical distribution over the eastern coast of the Red
111 Sea while lifting dust aerosols along the western slope of the Sarawat mountains, with the
112 elevated dust at a height of ~ 1.5 km over the mountains. Similarly, Talbot et al. (2007) observed
113 that enhanced turbulent activity along the SBF facilitated vertical aerosol transport above the
114 boundary layer top (~ 1.1 km a.s.l) over a flat coastal area of the North Sea.

115 Finally, high aerosol concentrations in the Houston area are linked to strong surface
116 emissions and meteorological conditions (Wert et al., 2003; Ryerson et al., 2003). This metro
117 region is also home to numerous petrochemical factories that are one of the sources of
118 anthropogenic emissions. Several studies have also shown that meteorological conditions
119 around Houston are highly susceptible to the interaction between large-scale (background)
120 geostrophic flows and mesoscale SBCs (Miller, 2003; Wang et al., 2024; Deng et al., 2025).
121 Pinto et al., (2014) observed that wind direction reversals bring aged, aerosol laden plumes
122 with high O_3 and NO_x levels back to the Houston area. They found that easterly winds,
123 originating from the Houston Ship Channel (HSC), are most strongly associated with elevated
124 levels of photochemically produced species. Similar conditions that promote O_3 and NO_x build-
125 up also drive secondary particle formation, leading to increases in aerosol number
126 concentrations. These particle-phase enhancements in total number concentration result in

127 higher aerosol concentration in the air mass transported from the east. Occasional increases in
128 aerosol concentrations around the greater Houston metropolitan area can also be associated
129 with long-range transported aerosols. At the synoptic scales, the circulation patterns modulate
130 regional meteorology over the Gulf coast. The Bermuda-Azores High helps trans-Atlantic
131 transport of North African dust to the southeast coast (Perry et al., 1997; Bozlaker et al., 2013).
132 Summertime conditions are notably influenced by episodic transboundary aerosol transport
133 (Mao et al., 2020; Das et al., 2023), including dust events from the Sahara Desert (Aldhaif et
134 al., 2020) and biomass burning events in Central America and its neighboring states. The
135 biomass burning includes prescribed agricultural fires in Central America (Wang et al., 2018)
136 and forest fires in surrounding states (Westenbarger and Morris, 2018). Central America
137 biomass burning contributes to half of the biomass burning particulate matter concentrations
138 in Houston (Das et al., 2023). The motivation of this study is to investigate the role of SAIs as
139 observed over a complex urban megacity region, and specifically document SBC influence on
140 aerosol microphysical properties. These efforts expand on previous air quality studies over
141 Houston, including Li et al. (2020) who employed a K-Means clustering algorithm to study the
142 relationship between Houston-region SBCs and the daily ozone variability during the
143 DISCOVER-AQ (Deriving Information on Surface Conditions from Column and Vertically
144 Resolved Observations Relevant to Air Quality) field campaign. While Li et al. (2020) focused
145 on gas-phase chemistry, the same emissions and meteorological processes that drive ozone
146 variability can also influence aerosol loading over the southern Texas region.

147 This study capitalizes on the TRacking Aerosol Convection Interactions ExpeRiment
148 (TRACER) field campaign conducted by the US Department of Energy (DOE) Atmospheric
149 Radiation Measurement (ARM) user facility (Mather and Voyles, 2013), which took place
150 from October 1, 2021, to September 30, 2022 (Jensen et al., 2022; 2025). The main TRACER
151 field site was placed at an urban coastal location in Houston. As in TRACER's overarching
152 motivations, the Houston region is frequented by isolated convective clouds that interact with
153 ambient aerosol conditions from the urban and industrial sources, potentially serving as a
154 natural contrast to clouds that form in surrounding areas that exhibit significantly lower
155 background aerosol concentrations (Banta et al., 2011; Parrish et al., 2009; Wang et al., 2024;
156 Thompson et al., 2025). Additional observations were made at a rural coastal site (supplemental
157 site) in southern Texas during an intensive observation period (IOP) from June 1 to September
158 30, 2022. Using these TRACER-IOP measurements, our study explores how these SBCs

159 influence the aerosol environment at multiple ground sites. In addition, the Weather Research
160 and Forecasting model coupled with Chemistry (WRF-Chem) is used to investigate the
161 regional impacts of SAI over Southern Texas. A detailed description of the TRACER sites,
162 instruments, measurements, and methodology, followed by the WRF-Chem model
163 configuration details, are presented in Section 2. Section 3 presents campaign observational
164 and simulated results. Our efforts will characterize the composite meteorological (Section 3.1)
165 and aerosol (Section 3.2) observations during the IOP at the TRACER main and supplemental
166 sites. This is followed by a composite analysis of the observed effects of the sea breeze on
167 aerosol properties at the two ARM sites (Section 3.3), as well as a detailed case study
168 examination of SAI influence for these locations (Section 3.4). The regional influence of SAI
169 is further explored using model simulations, as demonstrated for the horizontal (Section 3.5)
170 and vertical propagation of SAIs (Section 3.6), and SAI impact on cloud condensation nuclei
171 over the southern Texas region (Section 3.7). The study concludes with our key findings
172 summarized in Section 4.

173

174 **2 Data and methods**

175 2.1 Site description

176 The DOE ARM TRACER field campaign was centered on the deployment of the first ARM
177 Mobile Facility (Miller et al., 2016, herein AMF1) at the main instrument site (M1) (Fig. 1).
178 The M1 is an urban coastal site located at the La Porte, Texas (TX) airport, to the southeast of
179 Houston, TX. Given the high propensity for isolated convective cloud events during
180 summertime months (Jensen et al., 2022; 2025), the TRACER IOP was conducted from June
181 1 to September 30, 2022, with a goal towards sampling a range of aerosol-cloud interactions
182 during these convective events. Additional ARM and guest instruments were deployed to a
183 supplemental site (S3) during the IOP as documented in Jensen et al. (2022). The S3
184 supplemental site is a rural coastal site in Guy, TX, located ~70 km west from M1, upstream
185 and periphery to the highly populated and commercial sectors of the Houston-Galveston-
186 Brazoria region.

187 The southern Texas region is characterized by flat terrain with elevations < 50 m a.s.l and
188 a diversity of land cover/use, including urban, rural, grassland, and forested coastal

189 environments (see Fig. 2a). Although both the M1 and S3 sites are a similar distance from the
190 Gulf of Mexico, the M1 site is located near the western shore of Galveston Bay. This urban
191 M1 site may experience different sea-breeze timing because of its location, the added influence
192 of the Galveston Bay breeze, and urban heating that alters local circulations. The M1 site is
193 expected to be strongly influenced by anthropogenic activities due to its proximity to the
194 Houston urban core, large-scale industrial complexes and the HSC. The HSC is lined with
195 dense clusters of industrial facilities, including major petrochemical complexes (Yoon et al.,
196 2021), which can contribute to aerosol populations beyond those typically associated with an
197 urban environment. Similarly, the Texas A&M University (TAMU) TRACER measurements
198 also showed that short-lived ship emissions contributed to high aerosol concentrations (up to
199 $34,000 \text{ cm}^{-3}$) (Rapp et al., 2024; Thompson et al., 2025). The S3 site, while relatively less
200 impacted by the emissions from the Greater Houston area, is not representative of a pristine
201 rural location in terms of aerosol loading. Under typical south-southeasterly wind, this S3 site
202 is located downstream of heavy industry along the southeast Texas coastline (Freeport, TX and
203 Lake Jackson, TX) and can be influenced by upstream anthropogenic sources (Fig. 2b).

204

205 2.2 Measurements of aerosols and meteorological properties

206 This study focuses on the enhanced aerosol and complementary observations available
207 during the TRACER summertime IOP period. The key aerosol datasets available during this
208 IOP include: (1) the aerosol number size distribution and total number concentration, (2) bulk
209 aerosol chemical composition, and (3) state meteorological properties (e.g., surface
210 temperature, humidity). Campaign availability of in-situ observations at two contrasting sites
211 provided an excellent opportunity to understand the regional aspects of SAI.

212 The aerosol number size distribution with diameter ranging from 10 to 500 nm was
213 measured at M1 and S3 sites using Scanning Mobility Particle Sizer (SMPS) (Singh and Kuang,
214 2024). The aerosol number size distributions ($dN/d\log D_p$) (aerosol number concentrations in
215 different diameter bins) at different diameters (D_p) were added to calculate the total integrated
216 aerosol number concentrations. Bulk aerosol chemical compositions consisting of total
217 organics, sulfate, nitrate, ammonium, and chloride were measured at M1 and S3 sites using
218 Aerosol Chemical Speciation Monitor (ACSM) (Watson, 2017). Surface meteorological
219 variables: temperature, water vapor mixing ratio (w), wind direction and wind speed at M1 and

220 S3 sites were taken from the meteorological instruments collocated with the aerosol
221 instruments. All of these instruments are part of the ARM Aerosol Observing Systems (AOS),
222 which is the platform for in situ aerosol measurements at Earth's surface (Uin et al., 2019).
223 Missing data were excluded from this analysis. If more than 20% of the data were missing
224 during the 5 hours before and after the passing of the SBF, the dataset was not used to study
225 SAI processes. SMPS and ACSM sample data at 5-minute and ~30-minute intervals,
226 respectively. State meteorological variables were observed at one second intervals. All
227 datasets, except for the ACSM, were averaged over a 5-minute interval, centered on the time
228 of the SMPS sample.

229 To supplement the ARM observations, we use particulate matter of 2.5 micrometers or less
230 in diameter ($PM_{2.5}$) mass concentrations from the Texas Commission on Environmental
231 Quality (TCEQ) database (Shrestha et al., 2023; sfcmetradaq-tceq ARM PI product). Although
232 TCEQ operates a broad network of air quality monitoring stations throughout Texas, the
233 Seabrook Friendship Park site (C45, $-95.02^{\circ}E$, $29.58^{\circ}N$) was selected because it is the nearest
234 monitor to the M1 site (~6 km away) and provided continuous hourly $PM_{2.5}$ data during the
235 study period. $PM_{2.5}$ was chosen as a representative aerosol to directly compare with the model
236 simulations. For reference, this TCEQ C45 site location was added to the map displaying the
237 TRACER sites (Fig. 1).

238 This study draws heavily from SBC synoptic-scale regime identification performed by
239 Wang et al. (2024) to further inform on controls affecting SBC evolution and cloud formation
240 at the two sites. Every SBC day identified by Wang et al. (2024) during the IOP period is
241 considered to explore SAI during TRACER. A total of 46 SBC events at the M1 site, and 30
242 SB events at the S3 site were identified by Wang et al. (2024) during TRACER's IOP (Table
243 1). They explored Gulf breeze and bay breeze circulation characteristics using a suite of
244 datasets, including ground-based measurements, satellite observations, and reanalysis datasets,
245 using machine learning techniques, and Lagrangian cell tracking methods. Most IOP SBC
246 events were classified as occurring during large-scale anticyclonic conditions, with the
247 predominant occurrence of SBCs observed during southeasterly background surface wind
248 directions. The SBF timing at both ARM sites was determined using surface wind and w mixing
249 ratio time series.

250 Overall, Wang et al., (2024) found that the SBF typically arrived at the M1 site at 20:30
251 UTC (i.e., 15:30 LT), and at the S3 site at 20:50 UTC (i.e., 15:50 LT). The M1 site, situated

252 along the western shore of the Galveston Bay, was also influenced by bay breeze circulations,
253 frequently resulting in an earlier shift in the local meteorological state compared to that of the
254 S3 site (only influenced by the Gulf SBC). The M1 site was shown to experience an additional
255 bay breeze contribution during 22 out of 43 SBC events. Wang et al. (2024) also reported that
256 M1 experienced higher intensity changes in the meteorological conditions associated with these
257 SBFs as compared to S3, particularly when the background wind directions are southwesterly
258 or westerly. At both the sites, these SBF passages were associated with a significant increase
259 in w and wind speed, along with a decrease in surface temperature. The arrival of the fronts
260 also typically increased the vertical wind speed within the boundary layer, with a mean speed
261 of up to 2 m s^{-1} within the lowest 1 km. The enhanced updrafts associated with SBF low level
262 convergence also was shown to promote short lived-isolated convective clouds and likely
263 associated with vertical mixing of aerosols by diluting near-surface concentrations and
264 redistributing aerosols aloft.

265

266 2.3 Model simulation setup

267 The WRF-Chem model (Grell et al., 2005; Skamarock et al., 2008) was used to simulate
268 the multiscale interactions between aerosols and meteorology over the coastal region of
269 southeast Texas. Fig. 2 shows the model domain centered on the M1 site and extended from
270 26 to 33 °N (~770 km) in latitude and from -98.5 to -91.5 °E (~770 km) in longitude. The model
271 simulations were performed for the period from 1 July to 30 August 2022, using a 5x5 km
272 horizontal grid spacing with 45 vertical layers. A model spin-up time of 3 days was used, and
273 the restart files were used for the remainder of the simulations. Initial and boundary conditions
274 for meteorology were provided by the North American Mesoscale (NAM) model every 6 hours.
275 The model configuration was successfully set-up and is considered sufficient to resolve the key
276 meteorological processes relevant to the aerosol chemistry examined in this study. To validate
277 this assumption, simulated meteorological fields and aerosol variabilities are compared against
278 observations. Similar model setups have been successfully applied in previous WRF-Chem
279 studies over the continental US (e.g., Berg et al., 2015; Wang et al., 2021; Subba et al., 2023;
280 Shrivastava et al., 2024), which demonstrate their suitability for representing aerosol-cloud
281 interactions. The details of the configurations are shown in Table 2.

282 The model simulations were performed with (with aerosol-WA condition) and without (no
283 aerosol-NA condition) full aerosol-gas chemistry, and land-atmosphere interactions enabled.
284 Boundary conditions for gas-phase species and aerosols were provided by the Whole
285 Atmosphere Community Climate Model (WACCM) (Gettelman et al., 2019). The WACCM
286 output datasets, available on a horizontal grid resolution of $1^\circ \times 1^\circ$ were spatially interpolated
287 to our model domain every 6 hours. Biogenic emissions were generated online by WRF-Chem
288 model based on meteorology and land use data, using the Model of Emissions of Gases and
289 Aerosols from Nature version 2.1 (MEGAN2.1) by Guenther et al. (2012). The U.S.
290 Environmental Protection Agency National Emission Inventories (NEI, Ma and Tong, 2022)
291 was used to provide anthropogenic emissions of trace gases and aerosols from diverse sources,
292 including point, area, on-road mobile, non-road mobile, and other sectors. These emissions are
293 incorporated to WRF-Chem at hourly intervals. The area surrounding the M1 site is
294 characterized by urban infrastructure and cropland, whereas the S3 site is largely a mix of
295 cropland, natural mosaic, and barren or sparsely vegetated land type. Both sites have cropland
296 and grassland to the west and north, as well as evergreen, deciduous, and mixed forests from
297 the north to east directions. The selected domain included both anthropogenic and biogenic
298 aerosol sources, as indicated by NEI and MEGAN datasets (Fig. 2b). The M1 site is anticipated
299 to be more influenced by anthropogenic sources due to its proximity to the Houston urban core,
300 local industry and the HSC. The S3 site is expected to be more influenced by biogenic sources.

301 The role for these simulations is to provide a physically-reasonable spatial approximation
302 for the meteorological and aerosol environments across the southern Texas region that are not
303 captured by the point measurements during TRACER. Comparing the meteorological variables
304 between the two sites helps identify the underlying factors that may influence the aerosol
305 transport and transformation processes. The simulated meteorological time series show
306 adequate agreement for the purposes of this study at both sites (Fig. S1). We assessed model
307 performance using metrics: mean bias (MBE), root mean square error (RMSE), and correlation
308 coefficient (R) for the quantities of temperature, wind speed, and wind direction. In addition,
309 we also considered Modern-Era Retrospective analysis for Research and Applications
310 (MERRA-2) reanalysis products to further evaluate the model performance (Geralo et al.,
311 2017). Our model reproduces the measured temperature diurnal cycle at both sites with high
312 correlation (r up to 0.87) and low MBE ($< \pm 1$ °C). Wind speed and wind directions show
313 weaker correlation (r up to 0.65) and MBE of 0.76 m s^{-1} and 12.5° , respectively. Individual

314 SBF events are further analysed to compare the measured and modeled variables in later
315 sections.

316 We find a reasonable behavior in the heterogeneous spatial distribution of $PM_{2.5}$, with
317 higher values in the urban areas around the M1 site and lower values in the rural areas around
318 the S3 site (Fig. 3b). The simulated hourly $PM_{2.5}$ has been compared with the TCEQ measured
319 values (Fig. 3a). The model reasonably captures the timings and magnitude of high and low
320 aerosol concentrations. The model (mean $\sim 10.8 \mu\text{g m}^{-3}$, median $\sim 8.5 \mu\text{g m}^{-3}$) overestimates the
321 observations (mean $\sim 8.2 \mu\text{g m}^{-3}$, median $\sim 7.0 \mu\text{g m}^{-3}$), with a correlation of $r \sim 0.6$,
322 corresponding to differences of $\sim 30\%$ in the mean and $\sim 23\%$ in the median. These model-
323 measurement discrepancies are consistent with previously reported WRF-Chem biases. For
324 example, Soni et al. (2022) reported that during dust storm events over the Indian sub-
325 continent, WRF-Chem captured spatial aerosol patterns but underestimated concentrations in
326 regions of high aerosol loading. Similarly, Tuccella et al. (2012) reported that WRF-Chem
327 underestimated peak aerosol concentrations by 7.3%. More recently, Georgiou et al. (2022)
328 reported underestimation of background $PM_{2.5}$ by 16% and of industrial by $\sim 20\%$.

329

330 **3 Results and discussion**

331 **3.1 Composite IOP Meteorological Observations**

332 Comparisons between the background summertime meteorology around the TRACER
333 sites help to identify the underlying factors that may influence the aerosol transport and
334 transformation processes. Fig. 4. shows composite averaged diurnal variations of
335 meteorological properties during the IOP period. When comparing meteorological variables
336 between M1 and S3 sites, paired t-test results calculated a very low p-value (<0.0001) and a
337 large negative or positive t-statistic, indicating a statistically significant difference. M1 exhibits
338 higher temperatures during the cooler parts of the day (early morning) and slightly lower
339 temperatures during the warmest parts of the day (early afternoon). w is generally higher at M1
340 than at S3 for most hours of the day (Fig. 4b). At both sites the value stays near $17\text{-}18 \text{ g kg}^{-1}$
341 for most of the day, with a common moistening pulse around 13:00-15:00 UTC that coincides
342 with increased wind speed. At this time (13-15 UTC), the wind directions are similar at both
343 the sites. Except in the morning, winds at M1 are typically $1\text{-}2 \text{ m s}^{-1}$ stronger than at S3. The

344 M1 site shows an increase in w near 20:00 UTC, likely tied to the SBC. S3 exhibits a larger
345 shift in the wind directions compared to that of M1. The two sites have similar directions during
346 the late night (00:00- 05:00 UTC) and early morning (13:00-15:00 UTC) hours. During the
347 dominant afternoon SBC period (around 20:00 UTC), winds are predominantly from the
348 southeast at M1 and from the southwest at S3.

349 Although these sites are geographically close, their different proximities to water bodies
350 and varying land cover types may account for the observed meteorological variations, such as
351 differences in temperature modulation, humidity, and breeze development. M1 lies adjacent to
352 both Galveston Bay and Gulf of Mexico, thus nearby water moderates temperature and
353 promotes higher humidity, favoring sea- or bay- breeze circulations. In contrast, although S3
354 is at a similar distance from the Gulf as M1, it is more inland, separated from the shoreline by
355 an intervening expanse of land, so it experiences stronger daytime heating and a weaker, more
356 modified marine influence than M1. It has a land surface covered predominantly with
357 vegetation and soil that cools faster at night than urban landscapes. However, urban landscapes
358 retain heat, remaining warmer into the nighttime and potentially moderating temperatures
359 during the subsequent daytime (Maria et al., 2013). These behaviors are consistent with the
360 prior studies showing the coastal sites experienced moderate temperature and enhanced
361 humidity (Hu, 2021; Subramanian et al., 2023), and that land-use influenced local temperature
362 and boundary layer dynamics via evapotranspiration and surface heating (Fang et al., 2025).

363

364 3.2 Composite IOP Aerosol Observations

365 The southern Texas region is influenced by locally-generated (e.g., vehicular, industrial,
366 construction and road dust, and sea spray) and long range transported aerosols (e.g., biomass
367 burning, mineral dust, and sea spray) from anthropogenic and natural sources (Brown et al.,
368 2002; Barrett and Sheesley, 2014; Karnae and John, 2019; Song et al., 2021; Das et al., 2023;
369 Shrestha et al., 2023). In Fig. 5a, aerosol number concentration peaks around 17:00 UTC at M1
370 and around 20:00 UTC at S3. Both sites exhibit a tri-modal aerosol size distribution (Fig. 5b.).
371 Throughout the day, the aerosol concentrations are consistently higher at the M1 site when
372 compared to those observed at the S3 site. At the M1 site, we observe a distinct nucleation
373 mode that appears at diameter <20 nm, and two additional modes at larger diameters ~ 80 nm

374 and ~150 nm. This nucleation mode is less prominent at the S3 site, which more commonly
375 exhibits similar modes at diameters ~80 nm and ~150 nm.

376 The ACSM observations suggest a similar percentage contribution from various species,
377 with organics having the highest concentration (59.2% at M1 and 53.0% at S3), followed by
378 sulfate (23.3% at M1 and 30.6% at S3), ammonium (11.4% at M1 and 10.8% at S3), nitrate
379 (5.2% at M1 and 5.0% at S3) and chloride (less than 0.9% at M1, and less than 0.6% at S3).
380 Higher percentages of organics and sulfate were also measured at other urban (Minguillón et
381 al., 2015; Huang et al., 2010; Qi et al., 2020) and rural locations (Crippa et al., 2014; Atabakhsh
382 et al., 2023).

383 The NPF events are identified by analyzing the aerosol size distribution measured by the
384 SMPS (Kuang et al., 2008; Dal Maso et al., 2002; Mikkonen et al., 2011). This is accomplished
385 by designating characteristic features for NPF found in the size distribution behaviors in time,
386 including the appearance of the nucleation mode at a diameter (D_p) < 25 nm, followed by
387 distinct growth pattern (where the particles increase in size over several hours) forming the
388 characteristic “banana-shaped” pattern in the aerosol number size distribution. NPF events
389 were common at both the M1 and S3 sites. During summertime, NPF events were identified at
390 both the M1 and S3 sites, finding 23 and 17 events, respectively. In approximately 35% of
391 cases, NPF events were observed simultaneously at the sites, implying a regional-scale
392 behavior. These regional NPF nucleation modes appear at D_p < 25 nm and grow consistently
393 across a broader region, covering a minimum radius of tens of kilometers. Recent study by
394 Kasparoglu et al. (2025) also observed NPF events attributed to nucleation aloft with daytime
395 turbulent mixing transporting the growing mode downward, consistent with unsteady ultrafine
396 aerosol number concentrations, gradual increases, and absence of <20 nm growth near the
397 surface. The growing-mode hygroscopicity spanned 0.05-0.34, varied by wind sector,
398 implicating changes in precursor chemistry across air masses. Thus, the differing
399 characteristics of simultaneous NPF events are plausibly driven by mesoscale to large-scale
400 meteorological controls on these processes (such as SBCs), the prevailing condensation sink
401 from background aerosol, and/or the availability of precursors in each air mass.

402

403 3.3 Observed Sea Breeze aerosol interaction at the surface

404 Coastal regions have a mixture of urban, terrestrial, and marine aerosol regimes. The
405 inland-penetrating SBF can have a complex influence on the aerosol populations over Houston
406 and its surroundings depending on several coexisting factors including: (i) the pre-existing
407 aerosol regime over the location, (ii) the aerosol regime of the air mass preceded by the SBF,
408 (iii) the local to synoptic thermodynamic conditions resulting from convective boundary layer
409 features such as horizontal convective rolls, and (iv) the characteristics of the SBF itself,
410 including the lifting and mixing of the onshore flow with the ambient air, and wind anomalies
411 near the surface. Three scenarios for the influence of an inland-penetrating SBF on aerosols
412 within the region of influence are considered.

413 First, we consider a potential “reduction influence” that may occur when an air mass with
414 higher aerosol concentration over a location is replaced by an air mass with lower aerosol
415 concentration. In contrast, an “enhancement influence” may occur when an air mass with lower
416 aerosol concentration over a location is replaced by an air mass with higher aerosol
417 concentration. Otherwise, a “neutral influence” implies minimal change associated with the
418 SBF, defined as a change in the aerosol concentration is less than 5% in the pre-existing aerosol
419 regime. This scenario indicates that the air mass following the SBF is similar to the existing
420 conditions.

421 For example, these enhancement influence scenarios may be anticipated when long-range
422 transported aerosols are present in the air mass downwind of the SBF, or when the SBF first
423 advects over areas (marine or continental) with high local emissions. Similarly, neutral
424 influence scenarios are anticipated when the entire region has relatively homogeneous (i.e.,
425 similar aerosol concentrations also belonging to the same aerosol regime) distribution of
426 aerosols. Nevertheless, aerosol exchanges are complex, and TRACER also provided several
427 examples of marine aerosols carried by the SBF that were associated with negligible influences
428 on the ambient marine aerosol mode. Finally, TRACER site measurements may not always be
429 representative of a broader air mass or regional conditions (e.g., intermittent local source
430 interactions with smaller-scale SBC features). WRF-Chem modeling may help to bridge these
431 spatial representativeness gaps and provide reference for the regional context of the potential
432 impact of the SBC on aerosol distributions.

433 To investigate the influence of SAI, one approach employed in this study is to normalize
434 the surface aerosol concentration at time T by the value measured immediately before the
435 passing of the SBF ($T_{\text{SBF}}=0$ hour). The timing of the SBF for each event is explicitly

436 considered, using the passage times provided in Table A1 on Wang et al. (2024). The SBF
437 passage at a site is defined as $T_{\text{SBF}}=0$. This approach allowed evaluation of aerosol number
438 concentrations before and after the SBF passage while retaining the diurnal cycle context. Here,
439 “just before” refers to the five minutes prior to the SBF passage, as previously identified by
440 Wang et al. (2024). Figs. S2 and S3 show the temporal variation of this normalized aerosol
441 number concentration for all the SB events. At both the M1 and S3 sites, before-SBF aerosol
442 concentrations can vary by up to a factor of two.

443 Example days with an “enhancement influence” in the aerosol concentration after T_{SBF} are
444 shown in Fig. 6, highlighting the 18 July event at the M1 site, and a 10 August event at the S3
445 site. In contrast, the 17 June (M1 site) and 10 July (S3 site) events in the same figure help
446 illustrate a “reduction influence” in aerosol concentration after T_{SBF} . While these example
447 events are instructive, there is not a clear trend for TRACER events given the high level of
448 variability in the duration or influence of SAIs. For example, the sharp increase we observe in
449 aerosol concentration on the 10 August “enhancement” event quickly dissipates within an hour
450 after T_{SBF} at the S3 site. In contrast, the increase in the number concentration we observed on
451 18 July persisted for over an hour after T_{SBF} . Considering all the SBF passages we collected
452 (Figs. S2 and S3), we suggest $\Delta T = T_{\text{SBF}} \pm 1$ hour often best represents the “before” ($\Delta T = T_{\text{SBF}}$
453 - 1 hour) and “after”- SBF ($\Delta T = T_{\text{SBF}} + 1$ hour) times over a location. The enhancement or
454 reduction effects are most pronounced during the first hour following the passing of the SBF.
455 Beyond this period, the observed changes may be influenced by additional factors, such as the
456 secondary effects resulting from meteorological transitions induced by the SBF. Additionally,
457 the intensity of the SBF’s impact may begin to weaken or become less pronounced after the
458 first hour. With that assumption, a percentage change of the aerosol number concentration
459 $[(\text{after}-\text{before})/\text{before} \times 100\%]$ can be further calculated. ‘Neutral influence’ days with the
460 change in aerosol concentration $<10\%$ are not considered in this analysis.

461 Table 1 summarizes the total number of SBC events, along with number and percentage of
462 days showing enhancement, reduction, or neutral influence on the aerosol number
463 concentration at the M1 and S3 sites. Neutral days were excluded from the overall averages to
464 focus solely on the cases with a clear aerosol response. Out of 46 SBC events at the M1 site,
465 29 events (~63%) showed an enhancement or reduction influence on total aerosol number
466 concentration, while the remaining 17 events (~37%) were classified as having a neutral
467 influence. In contrast to M1, at the S3 site, out of 30 SBC events, only 12 events (~40%)

468 exhibited a detectable change in aerosol number concentration, with the remaining 18 days
469 (~60%) considered neutral. At the M1 site, reduction events (16 events) slightly outnumbered
470 enhancement events (13 events). In contrast, at S3, enhancements (8 events) were twice as
471 common as reductions (4 events). This opposite pattern underscores the site-dependent nature
472 of the sea-breeze influence.

473 During enhancement days, the M1 site shows an average increase in aerosol number
474 concentration of ~ 55%, rising from $3.8 \times 10^3 \text{ cm}^{-3}$ during ΔT^- to $5.9 \times 10^3 \text{ cm}^{-3}$ during ΔT^+ . In
475 contrast, during the reduction days, the concentration decreases by ~ 42%, dropping from $13.2 \times$
476 10^3 cm^{-3} during ΔT^- to $7.6 \times 10^3 \text{ cm}^{-3}$ during ΔT^+ . At the S3 site, the average changes are ~64%
477 (from $2.4 \times 10^3 \text{ cm}^{-3}$ during ΔT^- to $3.9 \times 10^3 \text{ cm}^{-3}$ during ΔT^+) enhancement and ~45% (from
478 $4.9 \times 10^3 \text{ cm}^{-3}$ during ΔT^- to $2.7 \times 10^3 \text{ cm}^{-3}$ during ΔT^+) reduction. When averaged across all
479 events, the aerosol number concentration at M1 shows a net decrease of ~23%, from 8.9×10^3
480 cm^{-3} during ΔT^- to $6.8 \times 10^3 \text{ cm}^{-3}$ during ΔT^+ , while S3 exhibits a net increase of ~9%, from
481 $3.2 \times 10^3 \text{ cm}^{-3}$ during ΔT^- to $3.5 \times 10^3 \text{ cm}^{-3}$. These contrasting trends underscore the regional
482 variability in aerosol responses associated with SAI events.

483 As previously mentioned, the geographical positioning of M1 and S3 sites could be one of
484 the reasons for such variabilities. M1 is more influenced by the bay breeze coming from
485 Galveston Bay and S3 is more likely influenced by Gulf breeze from Gulf of Mexico. Even if
486 the SBF air mass initially contains lower aerosol concentrations, a longer inland transit to S3
487 can (a) increase mixing with the preexisting continental boundary layer and (b) increase
488 acquisition of continental emissions along the over-land fetch, either of which can raise
489 concentrations by the time the SBF reaches S3, and vice versa. The M1 site is influenced by
490 the air masses and SBCs from both sources, whereas the S3 site is affected predominantly by
491 those originating from the Gulf of Mexico. As discussed in detail by previous studies (Sharma
492 et al., 2024; Wang et al., 2024), the SBFs originating from Galveston Bay and the Gulf of
493 Mexico are often distinct at onset but tend to merge later in the afternoon or evening. Due to
494 the M1 site's proximity to Galveston Bay, it is more directly influenced by maritime air masses
495 that are heavily modified by Galveston Bay as the SBF originating from the Gulf of Mexico
496 traverses the Bay. On the other hand, the Gulf-originating SBF must cross land before reaching
497 S3. The difference in SBF pathways can lead to notable meteorological and aerosol contrasts
498 between the two sites. In addition, as observed by Thompson et al. (2025), the maritime air
499 masses near Galveston can deviate significantly from typical clean maritime conditions. As a

500 result, bay breeze passages may not always lead to cleaner air but can, in fact, be more polluted.
501 The consequences of this increased aerosol concentration in the modified maritime air mass
502 are reflected in the enhancement aerosol response observed at the M1 site.

503 SAs can also interfere with NPF events. On SB days, a total of 7 NPF events were observed
504 at the M1 site and 4 at the S3 site, with 3 occurring simultaneously at both sites. Among these,
505 45% (5 out of 11) events showed distinct changes in NPF characteristics during the SBF
506 passage. For example, on 16 July an NPF event was observed at M1 prior to the SBF (Fig. S4).
507 With the arrival of the SBF, particle growth abruptly ceased, and the elevated particle
508 concentration ($\sim 14 \text{ e}^3 \text{ particles cm}^{-3}$) rapidly decreased to $\sim 5 \text{ e}^3 \text{ particles cm}^{-3}$ (Fig. S4). The
509 normalized aerosol size distribution further shows that the NPF activity evident in the hours
510 before the SBF period ($\Delta T = T_{\text{SBF}} - 1 \text{ hour}$) disappeared in the hour following the SBF
511 ($\Delta T = T_{\text{SBF}} + 1 \text{ hour}$). The low aerosol concentration air mass trailing the SBF passage thus led
512 to a sharp reduction in the aerosol number concentrations in the after-SBF period.

513 The open-air polar plots summarize the relationship between aerosol number concentration,
514 wind speed and wind direction within $\Delta T = T_{\text{SBF}} \pm 1 \text{ hour}$ during enhancement and reduction
515 events (Fig. 7). At M1, enhancement events reveal elevated aerosol concentrations when the
516 prevailing winds emanate from the east and southeast, where the air mass is influenced by
517 industry and shipping along Galveston Bay. During the reduction influence the pre-SBF aerosol
518 loading is higher compared to that of the reduction events. These high concentrations are
519 associated with the influence from the Houston urban core in the northwest and the other
520 influences from the east as mentioned above. These are also apparent in the monthly plots
521 shown in Fig. S5. After-SBF winds, particularly from the southeast and south, are associated
522 with markedly lower aerosol loads, indicative of cleaner marine air intrusion.

523 Meanwhile at S3, enhancement scenarios also manifest somewhat higher concentrations
524 when winds shift southeastward, though to a lesser extent, reflecting rural aerosol dynamics.
525 In reduction scenarios at S3, aerosol levels decrease most notably under southerly and
526 southwest flow, reinforcing the interpretation that sea breeze incursions generally replace
527 continental aerosol-laden air with cleaner marine air at both sites, albeit with stronger source
528 influence at M1. This wind-direction-dependent concentration pattern aligns with previous
529 findings: northwesterly to easterly winds bring continental aerosols, while southerly to
530 southwesterly flows usher in marine-influenced clean air that modulates aerosol number
531 concentrations (Levy et al., 2013; Pinto et al., 2014). Recent study by Kasparoglu et al. (2025)

532 observed that the cloud droplet number concentrations differed by a factor of ~ 2 -3 between
533 northeasterly and southerly flows, highlighting strong wind-direction controls on cloud
534 microphysics around southern Texas. However, as shown in Figs. S2 and S3, each SB event is
535 unique in terms of the change in the aerosol concentrations.

536

537 3.4. Examples of sea breeze aerosol interaction at the TRACER sites

538 In Fig. 8, we provide an example of an aerosol reduction influence of SAI. Since M1 and
539 S3 both experienced the passage of a SBF on 10 July, this day serves as a good example to
540 investigate how SAIs evolve when simultaneously viewed at multiple sites. The SBF reached
541 the M1 site in the afternoon at around 21:30 UTC, and the S3 site at around 23:45 UTC. In Fig.
542 S6, we supplement these discussions with displays for the temporal variation of measured and
543 model-simulated meteorological properties for this event. Both sites suggest the typical
544 temperature decreases and surface wind speed increase associated with the SBF reaching the
545 site. The wind direction changes from east to south at the M1 site and from southwest to south
546 at the S3 site.

547 The changes in aerosol size distribution, reduction in the bulk chemical composition, and
548 simulated $PM_{2.5}$ all suggest that the air mass following SBF passage contains lower aerosol
549 concentration (Fig. 8.). This likely indicates that during the after-SBF period, the air mass is
550 arriving from directions less influenced by the aerosol sources. The SBF acts as a leading edge
551 of this cleaner marine air mass. The aerosol number concentration decreases by $\sim 5\%$ (5.2 e^2
552 cm^{-3}) at the M1 site. At the M1 site, there was no significant change in the mean D_p ($\sim 100 \text{ nm}$)
553 during the first 45 min after T_{SBF} , which is followed by a sharp decrease in the mean D_p (~ 25
554 nm). This change in the aerosol number concentration is synchronous with the changes in wind
555 directions. During the after-SBF period, the winds shift predominantly from the southeast and
556 south, bringing in a more marine-influenced air mass.

557 Immediately after the passing of the SBF at the S3 site, the SAI also indicates a
558 reduction of the aerosol number concentration by $\sim 62\%$ ($3.3 \text{ e}^3 \text{ cm}^{-3}$) (Fig. 8b). However, the
559 background aerosol mode persists at diameters ~ 60 and 150 nm (aerosol size distribution plot
560 in Fig. 8b). Note, we did not observe a profound change in the wind directions after the passing
561 of the SBF at the S3 site. However, we suggest that the higher wind speed associated with the
562 SBF dilutes the existing air mass with marine air with lower aerosol concentration. Higher

563 wind speeds enhance near-surface shear, mechanically generate turbulence, deepen the
564 boundary layer, and strengthen vertical transport, thereby accelerating dispersion and diluting
565 aerosol and water-vapor concentrations (Kgabi and Mokgwetisi, 2009; Dueker et al., 2017; Liu
566 et al., 2025). Conversely, low winds with a shallow boundary layer and weak turbulence
567 promote accumulation and often worsen air quality due to limited dilution (Seinfeld and Pandis,
568 2006). The modified near-surface air mass at S3 persists overnight until convective mixing
569 begins the following day. Under stable stratification, buoyant turbulence is suppressed, and
570 shear-driven mixing becomes the primary dilution mechanism; although weaker than
571 convective mixing, it can still substantially mitigate concentration build-up (Rodier et al.,
572 2017).

573 The aerosol bulk chemical mass concentration at the M1 site shows a steady buildup
574 through the day, peaking just before the passing of the SBF. Organics were the dominant
575 species throughout, with sulfate and nitrate also contributing. After the passage of the SBF,
576 concentrations dropped rapidly by about 1 to 3 $\mu\text{g m}^{-3}$, with the drop being more apparent in
577 sulfate and organics. Within a few hours, concentrations returned to the background levels.
578 These concentrations remained higher than those at the rural S3 site. However, the more
579 pronounced changes in aerosol properties were observed at the S3 site. The concentrations of
580 all species, including organic, decreased by 2 to 3 $\mu\text{g m}^{-3}$. This is consistent with the earlier
581 discussion that the maritime air mass near Galveston Bay exhibits higher aerosol
582 concentrations compared to the more pristine maritime air mass originating directly from the
583 Gulf of Mexico.

584 In Figs. S7 and S8, we provide additional examples from TRACER SAI events. The first
585 example is from the 17 July event where we observed an increased influence in the aerosol
586 concentration that followed SBF passage. In Fig. S7, we present an example of an aerosol
587 enhancement case associated with an SAI event on 17 July. The SBF reached the M1 site in
588 the early afternoon (~18:12 UTC), and at around 21:42 UTC at the S3 site. The aerosol size
589 distribution displayed an enhancement of particles in the diameter range of 15-100 nm. Total
590 organics, sulfate, and simulated $\text{PM}_{2.5}$ also increased, suggesting that the post-SBF air mass
591 contained higher aerosol concentrations, likely due to transport from more polluted source
592 regions. Similar to the 10 July case, the SBF acted as the leading edge, but here it marked a
593 more polluted marine-influenced air mass.

594 At M1, the aerosol number concentration also doubled ($\sim 2.2 \times 10^3 \text{ cm}^{-3}$), accompanied by a
595 significant shift in mean particle diameter (within 15-100 nm) during the first hour after SBF
596 passage, with weaker changes thereafter. These responses were synchronous with shifts in wind
597 direction from southwest to east. The easterly winds, influenced by emissions from the HSC,
598 contributed to the observed increase. In contrast, at S3 the SAI did not produce distinct changes
599 in aerosol size distribution or mass concentrations, and except for the increase in the wind
600 speed, no substantial wind direction change occurred after SBF passage. The modified near-
601 surface air mass at both sites persisted for only ~ 2 hours, after which background conditions
602 returned. Notably, background aerosol modes at ~ 60 nm and ~ 150 nm persisted throughout
603 (Fig. S7).

604 Fig. S8 shows an example of a neutral SAI influence on 16 August. The SBF reached M1
605 at $\sim 17:05$ UTC and S3 at $\sim 20:10$ UTC. At M1, winds shifted from east to south, while no
606 distinct directional change was observed at S3. Unlike the 10 and 17 July cases, M1 was already
607 under high aerosol conditions, with particle concentrations consistently elevated at diameters
608 < 80 nm. In contrast, S3 remained under low aerosol conditions for most of the day, except for
609 a brief increase just prior to the SBF passage. The SAI did not produce notable changes in
610 aerosol size distribution, bulk chemical composition, or simulated $\text{PM}_{2.5}$, indicating that pre-
611 and post-SBF aerosol concentrations were comparable at both sites. Although wind direction
612 changed at M1, the marine-influenced air mass was also burdened by high aerosol loading,
613 limiting its impact on conditions at the site. Similarly, S3 showed no discernible change, with
614 concentrations remaining low before and after the SBF passage. Detailed discussions on these
615 example events will be continued in the next section that expands this discussion to include
616 regional removal and transport influences on these SAI events.

617

618 3.5. Regional influence of sea-breeze aerosol interaction

619 In Fig. 9, we provide the spatial distribution of modeled w , planetary boundary layer height
620 (PBLH), surface-level wind vectors, $\text{PM}_{2.5}$, and integrated aerosol number concentration
621 (nucleation- nu_0 + accumulation- ac_0 mode) using WRF-Chem. Together, nu_0 and ac_0
622 concentrations reveal size-dependent aerosol changes that bulk $\text{PM}_{2.5}$ mass or total number
623 obscure, allowing SBF-driven redistribution to be attributed to specific aerosol modes and
624 clarifying implications for microphysics, CCN/INP, and radiative effects. On 10 July, the

625 observed SBF reached the M1 site at 21:30 UTC and reached the S3 site at 23:45 UTC. The
626 simulation for this event accurately represents this timing for the SBF passage. The output for
627 the time 20:00 UTC on 10 July corresponds to an example point in the simulation and daytime
628 observations when the SBF had not reached either site. The 22:00 UTC examples correspond
629 to a time when the modeled and observed SBF has recently passed the M1 site but not reached
630 the S3 site. The 00:00 UTC examples (next day) correspond to a timing when the SBF has
631 passed both TRACER field sites.

632 Behind the SBF in our simulations, south or southeast winds prevail, passing through from
633 the Gulf of Mexico and blowing onshore at an average speed of 5 m s^{-1} . There is an increase in
634 w associated with the SBF passage. This transition in the air mass is also observed around the
635 M1 site at timestep 22:00 UTC. A similar pattern in the w is observed at the S3 site at the
636 timestep 00:00 UTC. This change at S3 is also accompanied by a decrease in the modeled
637 PBLH.

638 The 10 July simulations help illustrate that while changes in aerosol and meteorological
639 properties are more pronounced near the SBF, SBF influences may extend $>50 \text{ km}$ inland
640 associated with the path and extent of this feature. Along the convergence zone associated with
641 the SBF, particle concentrations are higher ahead of the SBF and lower behind it, due to
642 intrusion of cleaner marine air into the convergence zone. Consequently, SBF passage in the
643 model creates a swath of reduced aerosol concentration (up to 50%) parallel to the Galveston
644 Bay or Gulf of Mexico coastline. Over time, a well-defined dipole pattern emerges,
645 characterized by reduced concentrations over the coastal zone and enhanced concentrations
646 farther inland, consistent with the inland penetration of the maritime air mass and displacement
647 of pre-existing polluted air.

648 The additional example on 17 July (Fig. 10) is suggestive of an enhancement in aerosol
649 concentration associated with the SBF event, while the 16 August event (Fig. 11) is indicative
650 of a neutral influence from the SBF passage. Similar to 10 July, both days exhibit an increase
651 in w associated with passage of the SBF, relative to inland areas not influenced by the front
652 (Figs. 10a, 11a). The SBF passage was also accompanied by a decrease in modeled PBLH
653 (Figs. 10b, 11b). On 17 July, the SBF had reached M1 and S3 by $\sim 19:00$ and $21:00$ UTC,
654 respectively; winds were predominantly from southwest to east, with easterlies likely advecting
655 emissions from the HSC and contributing to the observed enhancements.

656 Notably, the 17 July event occurred in a different ambient aerosol environment than the 10
657 July event. MERRA-2 column dust mass concentrations (Fig. S9) indicate Saharan dust
658 transport on this day, yielding elevated dust loading over the Gulf of Mexico and resulting in
659 marine aerosol mass concentrations that exceeded those over land. The high concentrations are
660 also observed to be more prominent to the southwest of the M1 site (Fig. 10c). Hence, as the
661 SBF moves inland on 17 July, it transports this higher aerosol containing air mass, replacing
662 the lower aerosol containing air over the site and causing an increased aerosol concentration at
663 the M1 site. The onshore winds carry an air mass influenced by both local and long-range
664 transport, originating from both land and sea. In contrast to the other two events, the 16 August
665 event occurred under a transitional regime and likely influenced by the bay breeze. The aerosol
666 environment was notably uniform over the wider regional air masses, thus SBF passage
667 resulted in minimal changes to the aerosol distribution (Fig. 11c, d, f).

668 Overall, one implication from these simulations is that the effect of the inland-
669 penetrating SBF on the aerosol environment appears highly dependent on the pre-existing
670 aerosol condition over the location, as well as the air mass characteristics trailing the SBF. The
671 wind anomaly associated with the Gulf breeze front can transport more (less) polluted, particle-
672 laden air mass, leading to increased (decreased) aerosol concentration as it passes the site
673 during the subsequent ~5 hours after the front passes. A study by Deng et al., (2025) using
674 scanning radar data collected during TRACER reported similar findings during one of the SB
675 events on 10 September 2022. They reported a reduced influence on the aerosol concentration
676 immediately after the passing of the bay breeze front for the next few hours, due to the
677 dominance of onshore flow consistent with the findings from this study (Fig. S2).

678

679 3.6 Sea breeze effects on the vertical distribution of aerosols

680 Fig. 12 shows the modeled normalized $PM_{2.5}$ at different elevations before and after the
681 passage of the SBF. On 10 July, the cleaner marine air mass that follows the SBF led to a
682 decrease in aerosol concentration below 1 km at the ARM sites. The model indicates surface
683 convergence along the SBF (Fig. S10.). The aerosol concentrations are redistributed
684 horizontally and vertically. Two hours later, the SBF reaches the S3 site where its passage
685 causes a similar change in the aerosol concentration. The varying extent of this air mass and its
686 inland propagation redistributes the vertical $PM_{2.5}$ profiles from urban to suburban regions as

687 this SBF moves northwest from Houston. Similar to the changes in the aerosol mass
688 concentrations, the changes in the vertical distributions of nu_0 (Fig. 12b) and ac_0 number
689 concentration (Fig. 12c) are not homogeneous within these layers. The cleaner air mass
690 following the SBF replaces the more polluted continental air, lowering aerosol number
691 concentrations. The response is vertically inhomogeneous, reductions are most prominent
692 around M1 and are strongest below ~ 500 m. Within the 1.5 km, nu_0 shows the largest negative
693 anomalies (often $> 80\%$) immediately behind the SBF, consistent with marine air being
694 relatively depleted in the smallest particles. A thin narrow yellow/orange area ($\sim +70\%$
695 normalized changes) behind the front (within 1 to 1.5 km) reflects lifting, which can
696 momentarily concentrate or mix in small particles. The ac_0 exhibits a similar pattern but weaker
697 signal. This reflects that accumulation-mode particles are less sensitive to the front, so the
698 reductions are smaller and less uniform, with occasional localized decreases along the front.
699 Overall, the inland-propagating SBF drives an exchange between cleaner marine and more
700 polluted continental air masses, redistributing aerosols both horizontally and vertically.

701 These results complement those shown in SB simulations by Lu and Turco (1994),
702 Verma et al., (2006), Igel et al., (2018), and Parajuli et al., (2022). Parajuli et al., (2022)
703 observed that the SB pushes dust inland and upward along the mountain slopes, reaching
704 heights of up to 1.5 km. During TRACER, the vertical influence of SAI extended up to ~ 1.5
705 km (\sim PBLH). The region of SBC influence is shown to extend inland up to 50 km and vertically
706 up to 2 km over a period of up to 5 hours following the passage of the SBF. The model
707 simulations supplement the observations by filling observational gaps and enabling the
708 extrapolation of findings across a broader regional scale, an endeavor that would be challenging
709 to achieve with limited in-situ observational sites or standalone models.

710

711 3.7 Impacts of sea breeze aerosol interaction on cloud condensation nuclei

712 Fig. 13 shows the time series of the normalized aerosol number concentration with $D_p >$
713 100 nm, N_{100} for the 10 July event. Due to the unavailability of measured CCN data at both M1
714 and S3, N_{100} serves as our proxy for the CCN (CCN proxy) concentration (Ahlm et al., 2013).
715 Hence, the current analysis is limited to observational evidence of N_{100} variability. Similar to
716 the changes in the overall aerosol number budget, the SBF passage and the air mass that follows
717 induces simultaneous changes in the CCN budget. During this event, the CCN proxy

718 concentration decreases by ~35% at the M1 site and ~60% at the S3 site, with these changes
719 observed within an hour of the SBF passage.

720 Simulations performed for this event also suggest similar changes in aerosol budget,
721 indicating that the SBF brings in a cleaner air mass from directions consistent with a more
722 marine environment. Model results suggest that the CCN concentration at the surface decreases
723 by up to 60%, consistent with the observations. In our supplemental Figs. S11. and S12., we
724 include the temporal variation of the normalized N_{100} during all the other SB events during the
725 TRACER IOP. The preexisting N_{100} is less frequently impacted by the SAI than previous
726 examples we provided for SBF changes to the total number concentration, and these events
727 show a decrease in N_{100} for ~25% of the SB events at both M1 and S3 site. This suggests that
728 the influence of SAI is lesser over the marine influenced regional background aerosol larger
729 than 100 nm in diameter.

730

731 **4 Summary and conclusions**

732 Sea breezes influence multi-scale processes across the land-ocean-atmosphere interface
733 within the region of influence of the SBC. The TRACER field campaign provided a unique
734 opportunity to understand how aerosol and meteorological processes impact weather and
735 climate in the urban and rural coastal environment of Houston, Texas. A total of 46 (M1) and
736 30 (S3) instances of SB passages were identified during the summertime TRACER IOP period.
737 Summertime measurements from the ARM sites coupled with WRF-Chem model simulations
738 (July and August 2022) help to quantify aerosol changes resulting from onshore transport of
739 marine boundary layer air masses due to SBF passage and the associated atmospheric SBC
740 impacts.

741 Understanding the spatial extent and duration of SAIs is crucial for assessing their
742 environmental and meteorological impacts. For inland-penetrating SBFs, aerosol responses fall
743 into one of the three types: reduction (clean marine air replacing more polluted continental air);
744 enhancement (import of more polluted air), or neutral (similar air masses). The sign and
745 magnitude of changes depend on proximity to the coast, the upwind air mass history prior to
746 SBF arrival, and the antecedent airmass aerosol concentrations at each site.

747 TRACER measurements indicate that the urban M1 site, closer to both Galveston Bay
748 and the Gulf of Mexico, experiences more frequent aerosol concentration changes (increase or

749 decrease during 63% of SB events) than the rural S3 site (increase or decrease during 40% of
750 SB days), which is primarily Gulf-breeze influenced and farther from urban/industrial sources.
751 During IOP events, surface aerosol number changed by up to a factor of two. On average, SBF
752 passages were associated with a decrease of ~23% at M1 and increase of ~4% at S3. SBF
753 passages produce distinct aerosol responses depending on the type of SAI event. At M1,
754 enhancement days (28% of SB events) are associated with an average increase of aerosol
755 concentration by ~55%, while reduction days (35% of SB events) show an average decrease of
756 ~42%. At S3, enhancement days (27% of SB events) exhibit an average increase of ~64%,
757 whereas reduction days (13% of SB events) show a decrease of ~45%.

758 This study also provides support for how SAIs may interfere with aerosol microphysical
759 processes, including NPF events, a key driver of the overall aerosol number budget. These
760 changes occur with sharp meteorological shifts, including RH (+30%) and wind speed (+4 m
761 s⁻¹) increases, and backing to southeasterly flow (Figs. 7. and 8.). The relationship between
762 wind and aerosol number concentrations showed that aerosol concentrations at the M1 site are
763 higher when prevailing winds originate from the direction of the Houston urban core (northwest
764 to north), compared to the winds coming from the sea (south) (Fig. S5). Recently, Rapp et al.
765 (2024) emphasized using targeted mobile sampling that collecting measurements on both sides
766 of SB boundaries are critical for disentangling aerosol from meteorological controls. These
767 findings are complementary to the results in this study that boundary timing and air mass origin
768 drive the different responses at M1 and S3.

769 WRF Chem simulations extend the site perspective regionally, indicating
770 heterogeneous SAI footprints (Figs. 9, 10, 11, and 12). Across 18 simulated events, near surface
771 PM_{2.5} tends to decrease by ~15% around the M1 site and increase by ~3% near the S3 site (Fig.
772 S13). However, these responses vary with altitude (Fig. 12). The SBF may alter the vertical
773 aerosol distribution in the boundary layer up to 2 km. Beyond thermodynamics, SB fronts also
774 reshape convective environments (Wang et al., 2024). Thermodynamics and air mass across the
775 maritime and continental sides of these fronts influence storm characteristics and evolution
776 (Sharma et al., 2024).

777 With respect to cloud-relevant particles, both observations and simulations indicate that
778 the surface CCN proxy concentrations decrease by up to 60% following SBF passage (Fig. 13),
779 although such changes are infrequent (~25% of the SB events at both M1 and S3 site), implying
780 a weaker impact of SAI on marine influenced regional background accumulation mode. This

781 aligns with Thompson et al. (2025), which showed that aerosol cloud-forming properties differ
782 between polluted marine and continental air masses, with variability in size, hygroscopicity,
783 and CCN efficiency across sites. Given the complex mix of marine, terrestrial, and urban
784 sources, and the strong spatial heterogeneity revealed by both our analysis and prior TRACER
785 studies, future studies should include direct CCN and INP measurements and size-resolved
786 aerosol properties to better capture the role of SAI in aerosol–cloud interactions. It is important
787 to remember that these effects are localized, occurring only during shorter timescales (~5
788 hours) associated with daily SBC cycles over these locations. But these SAI timings align with
789 periods of peak solar radiation and elevated aerosol concentrations, potentially leading to
790 significant impacts on the radiation budget over the coastal regions. During times in close
791 proximity to SBF passage, changes in solar radiation and cloud formation may influence the
792 aerosol formation and distribution, modify atmospheric chemical reactions, and affect cloud
793 formation and properties, thereby impacting various atmospheric processes and interactions.
794 Because many coastal cities have high aerosol loading with frequent SBCs, accounting for SAI
795 when estimating direct aerosol radiative forcing is crucial. However, quantifying these changes
796 is challenging, underscoring the need for detailed future studies across diverse coastal regions.

797

798 **Code and data availability.** DOE-ARM datasets can be downloaded from the ARM data
799 discovery (https://adc.arm.gov//discovery/#/results/instrument_class_code::#). The TCEQ
800 data can be downloaded from <https://www.tceq.texas.gov/agency/data> and sfcmetradatq-tceq
801 ARM PI product (<https://doi.org/10.5439/2587278>) The Weather Research and Forecasting
802 Model with Chemistry model code is available from
803 www2.mmm.ucar.edu/wrf/users/download/. WRF-Chem preprocessors are available on the
804 website (www.aom.ucar.edu/wrf-chem). The model output data is made available upon
805 request. The primary tools to analyze the model output and generate figures are CDO
806 (code.mpimet.mpg.de/projects/cdo/), MATLAB (www.mathworks.com/products/), and
807 Jupyter Notebook platform (<https://jupyter.org>).

808

809 **Supplement.** The supplementary document contains supplementary figures referred to in the
810 main manuscript.

811

812 **Author contribution.** TS and CK planned the study; TS conducted the analysis and wrote the
813 manuscript; MH provided the aerosol data; MJ, MD, SG, MH, AS, DW, MZ and CK reviewed
814 and edited the manuscript.

815

816 **Competing interests.** The authors declare that they have no conflict of interest.

817

818 **Acknowledgments.** We would like to acknowledge support from the Atmospheric System
819 Research (ASR) program, the Atmospheric Radiation Measurement (ARM) user facility, and
820 the ARM TRACER operation and science teams. This research was supported in part by
821 resources provided by the National Energy Research Scientific Computing Center (NERSC),
822 a DOE Office of Science User Facility under Contract No. DE-AC02-05CH11231, through
823 NERSC award BER-ERCAP0026649. Additionally, the NE Linux Cluster (nlc) at Brookhaven
824 National Laboratory was utilized for model simulations and output storage.

825

826 **Financial support.** This paper has been authored by employees of Brookhaven Science
827 Associates, LLC, under Contract DE-SC0012704 with the U.S. Department of Energy (DOE).

828

829

830 **References**

831 Ackermann, I. J., Hass, H., Memmesheimer, M., Ebel, A., Binkowski, F. S., & Shankar, U.:
832 Modal aerosol dynamics model for Europe: Development and first applications.
833 Atmospheric Environment, 32(17), 2981–2999. [https://doi.org/10.1016/S1352-](https://doi.org/10.1016/S1352-2310(98)00006-5)
834 [2310\(98\)00006-5](https://doi.org/10.1016/S1352-2310(98)00006-5), 1998.

835 Adaricheva, K., Bernhardt, J. E., Liu, W., & Schmidt, B.: Importance of overnight parameters
836 to predict Sea Breeze on Long Island. <http://arxiv.org/abs/2309.01803>, 2023.

837 Ahlm, L., Junin, J., Fountoukis, C., Pandis, S. N., & Riipinen, I. (2013). Particle number
838 concentrations over Europe in 2030: The role of emissions and new particle formation.
839 Atmospheric Chemistry and Physics, 13(20), 10271–10283.
840 <https://doi.org/10.5194/acp-13-10271-2013>

841 Ahmadov, R., Gerbig, C., Kretschmer, R., Koerner, S., Neininger, B., Dolman, A. J., & Sarrat,
842 C.: Mesoscale covariance of transport and CO₂ fluxes: Evidence from observations and
843 simulations using the WRF-VPRM coupled atmosphere-biosphere model. *Journal of*
844 *Geophysical Research Atmospheres*, 112(22). <https://doi.org/10.1029/2007JD008552>,
845 2007.

846 Albrecht, B. A.: Aerosols, cloud microphysics, and fractional cloudiness. *Science*, 245, 1227–
847 1230, 1989.

848 Aldhaif, A. M., Lopez, D. H., Dadashazar, H., & Sorooshian, A.: Sources, frequency, and
849 chemical nature of dust events impacting the United States East Coast. *Atmospheric*
850 *Environment*, 231. <https://doi.org/10.1016/j.atmosenv.2020.117456>, 2020.

851 Ariya, P., Sun, J., Eltouny, N., Hudson, E. D., Hayes, C. T., & Kos, G.: Physical and chemical
852 characterization of bioaerosols—Implications for nucleation processes. *International*
853 *Reviews in Physical Chemistry*, 28(1), 1–32.
854 <https://doi.org/10.1080/01442350802597438>, 2009.

855 Arrillaga, J. A., Jiménez, P., de Arellano, J. V.-G., Jiménez, M. A., Román-Cascón, C., Sastre,
856 M., and Yagüe, C.: Analyzing the synoptic-, meso- and local-scale involved in sea
857 breeze formation and frontal characteristics. *J. Geophys. Res. Atmos.*, 125,
858 e2019JD031302, <https://doi.org/10.1029/2019JD031302>, 2020.

859 Atabakhsh, S., Poulain, L., Bigi, A., Coen, M. C., Pöhlker, M., & Herrmann, H.: Trends of
860 PM₁ aerosol chemical composition, carbonaceous aerosol, and source over the last 10
861 years at Melpitz (Germany). *Atmospheric Environment*, 346.
862 <https://doi.org/10.1016/j.atmosenv.2025.121075>, 2025.

863 Augustin, P., Billet, S., Crumeyrolle, S., Deboudt, K., Dieudonné, E., Flament, P., Fourmentin,
864 M., Guilbaud, S., Hanoune, B., Landkocz, Y., Méausoone, C., Roy, S., Schmitt, F. G.,
865 Sentchev, A., & Sokolov, A.: Impact of sea breeze dynamics on atmospheric pollutants
866 and their toxicity in industrial and urban coastal environments. *Remote Sensing*, 12(4).
867 <https://doi.org/10.3390/rs12040648>, 2020.

868 Banta, R. M., Senff, C. J., Alvarez, R. J., Langford, A. O., Parrish, D. D., Trainer, M. K., Darby,
869 L. S., Michael Hardesty, R., Lambeth, B., Andrew Neuman, J., Angevine, W. M.,
870 Nielsen-Gammon, J., Sandberg, S. P., & White, A. B.: Dependence of daily peak O₃
871 concentrations near Houston, Texas on environmental factors: Wind speed,

872 temperature, and boundary-layer depth. *Atmospheric Environment*, 45(1), 162–173.
873 <https://doi.org/10.1016/j.atmosenv.2010.09.030>, 2011.

874 Bao, S., Pietrafesa, L., Gayes, P., Noble, S., Viner, B., Qian, J. H., Werth, D., Mitchell, G., &
875 Burdette, S.: Mapping the Spatial Footprint of Sea Breeze Winds in the Southeastern
876 United States. *Journal of Geophysical Research: Atmospheres*, 128(7).
877 <https://doi.org/10.1029/2022JD037524>, 2023.

878 Barrett, T. E., & Sheesley, R. J.: Urban impacts on regional carbonaceous aerosols: Case study
879 in central Texas. *Journal of the Air and Waste Management Association*, 64(8), 917–
880 926. <https://doi.org/10.1080/10962247.2014.904252>, 2014.

881 Bauman, W. H.: Verify MesoNAM Performance. NASA Contractor Report CR-2010-216-287,
882 Kennedy Space Center, FL, 31 pp. [Available from ENSCO, Inc., 1980 N. Atlantic
883 Ave., Suite 830, Cocoa Beach, FL, 32931 and online at
884 <http://science.ksc.nasa.gov/amu/final-reports/mesoNAMverify.pdf>.], 2010.

885 Bond, T. C., Doherty, S. J., Fahey, D. W., Forster, P. M., Berntsen, T., Deangelo, B. J., Flanner,
886 M. G., Ghan, S., Kärcher, B., Koch, D., Kinne, S., Kondo, Y., Quinn, P. K., Sarofim,
887 M. C., Schultz, M. G., Schulz, M., Venkataraman, C., Zhang, H., Zhang, S., ... Zender,
888 C. S.: Bounding the role of black carbon in the climate system: A scientific assessment.
889 *Journal of Geophysical Research Atmospheres*, 118(11), 5380–5552.
890 <https://doi.org/10.1002/jgrd.50171>, 2013.

891 Borge, R., Alexandrov, V., José del Vas, J., Lumberras, J., & Rodríguez, E.: A comprehensive
892 sensitivity analysis of the WRF model for air quality applications over the Iberian
893 Peninsula. *Atmospheric Environment*, 42(37), 8560–8574.
894 <https://doi.org/10.1016/j.atmosenv.2008.08.032>, 2008.

895 Boyer, C. H., Keeler, J. M., & Rakoczy, B. C. (2025). An Idealized Parameter Study of
896 Destabilization and Convection Initiation in Coastal Regions. Part I: Calm or Offshore
897 Synoptic-Scale Flow. *Journal of the Atmospheric Sciences*, 82(3), 519–539.
898 <https://doi.org/10.1175/JAS-D-23-0180.1>

899 Boyouk, N., Léon, J. F., Delbarre, H., Augustin, P., & Fourmentin, M.: Impact of sea breeze
900 on vertical structure of aerosol optical properties in Dunkerque, France. *Atmospheric*
901 *Research*, 101(4), 902–910. <https://doi.org/10.1016/j.atmosres.2011.05.016>, 2011.

- 902 Bozlaker, A., Prospero, J. M., Fraser, M. P., & Chellam, S.: Quantifying the contribution of
903 long-range saharan dust transport on particulate matter concentrations in Houston,
904 Texas, using detailed elemental analysis. *Environmental Science and Technology*,
905 47(18), 10179–10187. <https://doi.org/10.1021/es4015663>, 2013.
- 906 Brown, S., Nicholls, R. J., Woodroffe, C. D., Hanson, S., Hinkel, J., Kebede, A. S., Neumann,
907 B. and Vafeidis, A. T.: “Sea-Level Rise Impacts and Responses: A Global Perspective.”
908 In *Coastal Hazards*, edited by Charles W. Finkl, 117–49. Dordrecht: Springer
909 Netherlands. https://doi.org/10.1007/978-94-007-5234-4_5, 2013.
- 910 Burkart, J., Gratzl, J., Seifried, T. M., Bieber, P., & Grothe, H.: Subpollen particles (SPP) of
911 birch as carriers of ice nucleating macromolecules. *Biogeosciences Discussions*, 1–15,
912 2021.
- 913 Charlson, R. J., Schwartz, S. E., Hales, J. M., Cess, R. D., Coakley, J. A. Jr, Hansen, J. E., and
914 Hofmann, D. J.: Climate forcing by anthropogenic aerosols. *Science* 255, 423–430,
915 1992.
- 916 Chen, F., & Dudhia, J.: Coupling an advanced land surface-hydrology model with the Penn
917 State-NCAR MM5 modeling system. Part I: Model implementation and sensitivity.
918 *Monthly Weather Review*, 129(4), 569–585. [https://doi.org/10.1175/1520-
919 0493\(2001\)129<0569:caalsh>2.0.co;2](https://doi.org/10.1175/1520-0493(2001)129<0569:caalsh>2.0.co;2), 2001.
- 920 Chou, M., Suarez, M. J., Ho, C., Yan, M. M., & Lee, K.: Parameterizations for cloud
921 overlapping and shortwave single-scattering properties for use in general circulation
922 and cloud ensemble models. *Journal of Climate*, 11(2), 202–214. [https://doi.
923 org/10.1175/1520-0442\(1998\)011<0202:PFCOAS>2.0.CO;2](https://doi.org/10.1175/1520-0442(1998)011<0202:PFCOAS>2.0.CO;2), 1998.
- 924 Clappier, A., Martilli, A., Grossi, P., Thunis, P., Pasi, F., Krueger, B. C., Calpini, B., &
925 Graziani, G., Bergh, H.V.D.: Effect of Sea Breeze on Air Pollution in the Greater
926 Athens Area. Part I: Numerical Simulations and Field Observations. *J. of Applied
927 meteorology*, (39). [https://doi.org/10.1175/1520-
928 0450\(2000\)039<0546:EOSBOA>2.0.CO;2](https://doi.org/10.1175/1520-0450(2000)039<0546:EOSBOA>2.0.CO;2), 1999.
- 929 Comin, A. N., Miglietta, M. M., Rizza, U., Acevedo, O. C., & Degrazia, G. A.: Investigation
930 of sea-breeze convergence in Salento Peninsula (southeastern Italy). *Atmospheric
931 Research*, 160, 68–79. <https://doi.org/10.1016/j.atmosres.2015.03.010>, 2015.

932 Crippa, M., Canonaco, F., Lanz, V. A., Äijälä, M., Allan, J. D., Carbone, S., Capes, G.,
933 Ceburnis, D., Dall'Osto, M., Day, D. A., DeCarlo, P. F., Ehn, M., Eriksson, A., Freney,
934 E., Hildebrandt Ruiz, L., Hillamo, R., Jimenez, J. L., Junninen, H., KiendlerScharr, A.,
935 Kortelainen, A. M., Kulmala, M., Laaksonen, A., Mensah, A. A., Mohr, C., Nemitz, E.,
936 O'Dowd, C., Ovadnevaite, J., Pandis, S. N., Petäjä, T., Poulain, L., Saarikoski, S.,
937 Sellegri, K., Swietlicki, E., Tiitta, P., Worsnop, D. R., Baltensperger, U., Prévôt, A. S.
938 H.: Organic aerosol components derived from 25 AMS data sets across Europe using a
939 consistent ME-2 based source apportionment approach. *Atmos. Chem. Phys.* 14 (12),
940 6159–6176. <https://doi.org/10.5194/acp-14-6159>, 2014.

941 Crossett, K., Culliton, T., Wiley, P., & Goodspeed, T.: Population trends along the coastal
942 United States, 1980–2008. Silver Spring, National Oceanic and Atmospheric
943 Administration, 2004.

944 Das, S., Prospero, J. M., & Chellam, S.: Quantifying international and interstate contributions
945 to primary ambient PM_{2.5} and PM₁₀ in a complex metropolitan atmosphere.
946 *Atmospheric Environment*, 292. <https://doi.org/10.1016/j.atmosenv.2022.119415>,
947 2023.

948 Deng, Min, et al.: A Closed Bay-Breeze Circulation and Its Lifecycle from TRACER with a
949 New Orienteering Tape Recorder Diagram, *Journal of Geophysical Research:*
950 *Atmospheres* (under revision), 2025.

951 di Bernardino, A., Iannarelli, A. M., Casadio, S., Mevi, G., Campanelli, M., Casasanta, G.,
952 Cede, A., Tiefengraber, M., Siani, A. M., Spinei, E., & Cacciani, M.: On the effect of
953 sea breeze regime on aerosols and gases properties in the urban area of Rome, Italy.
954 *Urban Climate*, 37. <https://doi.org/10.1016/j.uclim.2021.100842>, 2021.

955 Emmons, L. K., Walters, S., Hess, P. G., Lamarque, J. F., Pfister, G. G., Fillmore, D., et al.:
956 Description and evaluation of the model for ozone and related chemical tracers, version
957 4 (MOZART-4). *Geoscientific Model Development*, 3(1), 43–67.
958 <https://doi.org/10.5194/gmd-3-43-2010>, 2010.

959 Dueker, M. E., O'Mullan, G. D., Martínez, J. M., Juhl, A. R., & Weathers, K. C.: Onshore
960 wind speed modulates microbial aerosols along an urban waterfront. *Atmosphere*,
961 8(11). <https://doi.org/10.3390/atmos8110215>, 2017.

962 Fang, C., Li, X., Li, J., Tian, J., & Wang, J. (2025). Research on the impact of land use and
963 land cover changes on local meteorological conditions and surface ozone in the north
964 China plain from 2001 to 2020. *Scientific Reports*, 15(1).
965 <https://doi.org/10.1038/s41598-025-85940-0>

966 Gangoiti, G., Millán, M. M., Salvador, R., & Mantilla, E.: Long-range transport and re-
967 circulation of pollutants in the western Mediterranean during the project Regional
968 Cycles of Air Pollution in the West-Central Mediterranean Area. *Atmospheric*
969 *Environment*, 35(36), 6267–6276. [https://doi.org/10.1016/S1352-2310\(01\)00440-X](https://doi.org/10.1016/S1352-2310(01)00440-X),
970 2001.

971 Gelaro, R., and Coauthors: The Modern-Era Retrospective Analysis for Research and
972 Applications, version 2 (MERRA-2). *J. Climate*, 30, 5419–5454,
973 <https://doi.org/10.1175/JCLI-D-16-0758.1>, 2017.

974 Georgiou, G. K., Christoudias, T., Proestos, Y., Kushta, J., Pikridas, M., Sciare, J., Savvides,
975 C., & Lelieveld, J.: Evaluation of WRF-Chem model (v3.9.1.1) real-Time air quality
976 forecasts over the Eastern Mediterranean. *Geoscientific Model Development*, 15(10),
977 4129–4146. <https://doi.org/10.5194/gmd-15-4129-2022>, 2022.

978 Gettelman, A., Mills, M. J., Kinnison, D. E., Garcia, R. R., Smith, A. K., Marsh, D. R., et al.:
979 The whole atmosphere community climate model version 6 (WACCM6). *Journal of*
980 *Geophysical Research: Atmospheres*, 124, <https://doi.org/10.1029/2019JD030943>,
981 2019.

982 Glantz, P., Nilsson, D. E., & von Hoyningen-Huene, W. (2006). Estimating a relationship
983 between aerosol optical thickness and surface wind speed over the ocean. In *Atmos.*
984 *Chem. Phys. Discuss* (Vol. 6). www.atmos-chem-phys-discuss.net/6/11621/2006/

985 Grell, G. A., & Devenyi, D.: A generalized approach to parameterizing convection combining
986 ensemble and data assimilation techniques. *Geophysical Research Letters*, 29(4), 38-1–
987 38-4. <https://doi.org/10.1029/2002GL015311>, 2002.

988 Grell, G. A., Peckham, S. E., Schmitz, R., McKeen, S. A., Frost, G., Skamarock, W. C., &
989 Eder, B.: Fully coupled “online” chemistry within the WRF model. *Atmospheric*
990 *Environment*, 39(37), 6957–6975. <https://doi.org/10.1016/j.atmosenv.2005.04.027>,
991 2005.

- 992 Guenther, A. B., Jiang, X., Heald, C. L., Sakulyanontvittaya, T., Duhl, T., Emmons, L. K., &
993 Wang, X.: The model of emissions of gases and aerosols from nature version 2.1
994 (MEGAN2.1): An extended and updated framework for modeling biogenic emissions.
995 *Geoscientific Model Development*, 5(6), 1471–1492. [https://doi.org/10.5194/gmd-5-](https://doi.org/10.5194/gmd-5-1471-2012)
996 1471-2012, 2012.
- 997 Hanft, W., & Houston, A. L.: An Observational and Modeling Study of Mesoscale Air Masses
998 with High Theta-E. <https://doi.org/10.1175/MWR-D-17>, 2018.
- 999 Hernández-Ceballos, M. A., Sorribas, M., San Miguel, E. G., Cinelli, G., Adame, J. A., &
1000 Bolívar, J. P.: Impact of sea-land breezes on 210Pb in southern Iberian Peninsula–
1001 Feasibility study on using submicron-sized aerosol particles to analyze 210Pb hourly
1002 patterns. *Atmospheric Pollution Research*, 7(1), 1–8.
1003 <https://doi.org/10.1016/j.apr.2015.06.011>, 2016.
- 1004 Hong, S. Y., Noh, Y., & Dudhia, J.: A new vertical diffusion package with an explicit treatment
1005 of entrainment processes. *Monthly Weather Review*, 134(9), 2318–2341.
1006 <https://doi.org/10.1175/MWR3199.1>, 2006.
- 1007 Hu, L. (2021). A Global Assessment of Coastal Marine Heatwaves and Their Relation With
1008 Coastal Urban Thermal Changes. *Geophysical Research Letters*, 48(9).
1009 <https://doi.org/10.1029/2021GL093260>
- 1010 Huang, X. F., He, L. Y., Hu, M., Canagaratna, M. R., Sun, Y., Zhang, Q., Zhu, T., Xue, L.,
1011 Zeng, L. W., Liu, X. G., Zhang, Y. H., Jayne, J. T., Ng, N. L., Worsnop, D. R.: Highly
1012 time-resolved chemical characterization of atmospheric submicron particles during
1013 2008 Beijing Olympic Games using an Aerodyne High-Resolution Aerosol Mass
1014 Spectrometer. *Atmos. Chem. Phys.* 2010, 10, 8933–8945, DOI: 10.5194/acp-10-8933-
1015 2010.
- 1016 Hudson, B.: Coastal Land Loss and the Mitigation-Adaptation Dilemma: Between Scylla and
1017 Charybdis Repository Citation Coastal Land Loss and the Mitigation-Adaptation
1018 Dilemma: Between Scylla and Charybdis. In *Louisiana Law Review* (Vol. 73).
1019 <https://digitalcommons.law.lsu.edu/lalrev/vol73/iss1/3>, 2012.
- 1020 Igel, A. L., van den Heever, S. C., & Johnson, J. S.: Meteorological and Land Surface
1021 Properties Impacting Sea Breeze Extent and Aerosol Distribution in a Dry

- 1022 Environment. *Journal of Geophysical Research: Atmospheres*, 123(1), 22–37.
1023 <https://doi.org/10.1002/2017JD027339>, 2018.
- 1024 IPCC, Intergovernmental Panel on Climate Change: In V. Masson-Delmotte, P. Zhai, A.
1025 Pirani, S. L. Connors, C. P. an, S. Berger, et al. (Eds.), *The Physical Science Basis.*
1026 *Contribution of Working Group I to the Sixth Assessment Report of the*
1027 *Intergovernmental Panel on Climate Change.* Cambridge University Press.
1028 <https://doi.org/10.1017/9781009157896>, 2021.
- 1029 Iwai, H., Murayama, Y., Ishii, S., Mizutani, K., Ohno, Y., & Hashiguchi, T.: Strong Updraft at
1030 a Sea-Breeze Front and Associated Vertical Transport of Near-Surface Dense Aerosol
1031 Observed by Doppler Lidar and Ceilometer. *Boundary-Layer Meteorology*, 141(1),
1032 117–142. <https://doi.org/10.1007/s10546-011-9635-z>, 2011.
- 1033 Janjic, Z. I.: Nonsingular implementation of the Mellor–Yamada level 2.5 scheme in the NCEP
1034 Meso model. *NCEP Office Note*, 437, 61, 2002.
- 1035 Jensen, M. P., and Coauthors, (2022): A Succession of Cloud, Precipitation, Aerosol, and Air
1036 Quality Field Experiments in the Coastal Urban Environment. *Bull. Amer. Meteor.*
1037 *Soc.*, 103, 103–105, <https://doi.org/10.1175/BAMS-D-21-0104.1>, 2022.
- 1038 Jensen, M. P., Flynn, J. H., Gonzalez-Cruz, J. E., Judd, L. M., Kollias, P., Kuang, C.,
1039 McFarquhar, G. M., Powers, H., Ramamurthy, P., Sullivan, J., Aiken, A. C., Alvarez,
1040 S. L., Argay, P., Argrow, B., Bell, T. M., Boyer, D., Brooks, S. D., Bruning, E. C.,
1041 Brunner, K., ... Zhu, Z. (2025). Studying Aerosol, Clouds, and Air Quality in the
1042 Coastal Urban Environment of Southeastern Texas. *Bulletin of the American*
1043 *Meteorological Society*. <https://doi.org/10.1175/bams-d-23-0331.1>
- 1044 Karnae, S., & John, K.: Source apportionment of PM_{2.5} measured in South Texas near U.S.A.
1045 – Mexico border. *Atmospheric Pollution Research*, 10(5), 1663–1676.
1046 <https://doi.org/10.1016/j.apr.2019.06.007>
- 1047 Kasparoglu, S., Meskhidze, N., & Petters, M. D. (2024). Aerosol mixing state, new particle
1048 formation, and cloud droplet number concentration in an urban environment. *Science*
1049 *of the Total Environment*, 951. <https://doi.org/10.1016/j.scitotenv.2024.175307>
- 1050 Kerminen, V. M., Chen, X., Vakkari, V., Petäjä, T., Kulmala, M., & Bianchi, F. : Atmospheric
1051 new particle formation and growth: Review of field observations. In *Environmental*

1052 Research Letters (Vol. 13, Issue 10). Institute of Physics Publishing.
1053 <https://doi.org/10.1088/1748-9326/aadf3c>, 2018.

1054 Kgabi, N. A., & Mokgwetsi, T. (2009). Dilution and dispersion of inhalable particulate matter.
1055 WIT Transactions on Ecology and the Environment, 127, 229–238.
1056 <https://doi.org/10.2495/RAV090201>

1057 Kleinman, L. I., Daum, P. H., Imre, D. G., Lee, Y.-N., Nunnermacker, L. J., Springston, S. R.,
1058 Weinstein-Lloyd, J., and Rudolph, J.: Ozone production rate and hydrocarbon reactivity
1059 in 5 urban areas: A cause of high ozone concentration in Houston, Geophys. Res. Lett.,
1060 29(10), 1467, doi:10.1029/2001GL014569, 2002.

1061 Kuang, C., Chen, M., Zhao, J., Smith, J., McMurry, P. H., & Wang, J.: Size and time-resolved
1062 growth rate measurements of 1 to 5 nm freshly formed atmospheric nuclei. Atmospheric
1063 Chemistry and Physics, 12(7), 3573–3589. <https://doi.org/10.5194/acp-12-3573-2012>,
1064 2012.

1065 Kuang, C., McMurry, P. H., and McCormick, A. V.: Determination of cloud condensation
1066 nuclei production from measured new particle formation events, Geophys. Res. Lett.,
1067 36, L09822, doi:10.1029/2009GL037584, 2009.

1068 Kulmala, M., Laakso, L., Lehtinen, K. E. J., Riipinen, I., Dal Maso, M., Anttila, T., Kerminen,
1069 V.-M., Horrak, U., Vana, M., and Tammet, H.: Initial steps of aerosol growth, Atmos.
1070 Chem. Phys., 4, 2553–2560, doi:10.5194/acp-4-2553-2004, 2004.

1071 Kulmala, M., Petäjä, T., Ehn, M., Thornton, J., Sipilä, M., Worsnop, D. R., & Kerminen, V.
1072 M.: Chemistry of atmospheric nucleation: On the recent advances on precursor
1073 characterization and atmospheric cluster composition in connection with atmospheric
1074 new particle formation. Annual Review of Physical Chemistry, 65, 21–37.
1075 <https://doi.org/10.1146/annurev-physchem-040412-110014>, 2014.

1076 Levy, M. E., Zhang, R., Khalizov, A. F., Zheng, J., Collins, D. R., Glen, C. R., Wang, Y., Yu,
1077 X. Y., Luke, W., Jayne, J. T., & Olaguer, E.: Measurements of submicron aerosols in
1078 Houston, Texas during the 2009 SHARP field campaign. Journal of Geophysical
1079 Research Atmospheres, 118(18), 10,518-10,534. <https://doi.org/10.1002/jgrd.50785>,
1080 2013.

- 1081 Li, W., Wang, Y., Bernier, C., & Estes, M.: Identification of Sea Breeze Recirculation and Its
1082 Effects on Ozone in Houston, TX, During DISCOVER-AQ 2013. *Journal of*
1083 *Geophysical Research: Atmospheres*, 125(22). <https://doi.org/10.1029/2020JD033165>,
1084 2020.
- 1085 Linden, P.F., Simpson, J.E., Gravity-driven flows in a turbulent fluid. *Journal of Fluid*
1086 *Mechanics*,172, 481-497. doi:10.1017/S0022112086001829, 1986.
- 1087 Liu, H., Zhang, B., Moore, R. H., Ziemba, L. D., Ferrare, R. A., Choi, H., Sorooshian, A.,
1088 Painemal, D., Wang, H., Shook, M. A., Scarino, A. J., Hair, J. W., Crosbie, E. C., Fenn,
1089 M. A., Shingler, T. J., Hostetler, C. A., Chen, G., Kleb, M. M., Luo, G., ... Johnson,
1090 M. S.: Tropospheric aerosols over the western North Atlantic Ocean during the winter
1091 and summer deployments of ACTIVATE 2020: Life cycle, transport, and distribution.
1092 *Atmospheric Chemistry and Physics*, 25(4), 2087–2121. [https://doi.org/10.5194/acp-](https://doi.org/10.5194/acp-25-2087-2025)
1093 [25-2087-2025](https://doi.org/10.5194/acp-25-2087-2025), 2025.
- 1094 Lu, R., & Turco, R. P.: Air pollutant transport in a coastal environment.1. 2-dimensional
1095 simulations of sea-breeze and mountain effects. *Journal of the Atmospheric Sciences*,
1096 51(15), 2285–2308. [https://doi.org/10.1175/1520-](https://doi.org/10.1175/1520-0469(1994)051<2285:APTIAC>2.0.CO;2)
1097 [0469\(1994\)051<2285:APTIAC>2.0.CO;2](https://doi.org/10.1175/1520-0469(1994)051<2285:APTIAC>2.0.CO;2), 1994.
- 1098 Ma, S., & Tong, D. Q.: Neighborhood Emission Mapping Operation (NEMO): A 1-km
1099 anthropogenic emission dataset in the United States. *Scientific Data*, 9(1).
1100 <https://doi.org/10.1038/s41597-022-01790-9>, 2022.
- 1101 Mack, S. M., Madl, A. K., & Pinkerton, K. E.: Respiratory health effects of exposure to ambient
1102 particulate matter and bioaerosols. *Comprehensive Physiology*, 10(1), 1–20.
1103 <https://doi.org/10.1002/cphy.c180040>, 2020.
- 1104 Mao, F., Zang, L., Wang, Z., Pan, Z., Zhu, B., & Gong, W.: Dominant synoptic patterns during
1105 wintertime and their impacts on aerosol pollution in Central China. *Atmospheric*
1106 *Research*, 232. <https://doi.org/10.1016/j.atmosres.2019.104701>, 2020.
- 1107 Maria, V. D., Rahman, M., Collins, P., Dondi, G., & Sangiorgi, C. (2013). Urban Heat Island
1108 Effect: Thermal Response from Different Types of Exposed Paved Surfaces.
1109 *International Journal of Pavement Research and Technology*, 6(4), 414-422.
1110 [https://doi.org/10.6135/ijprt.org.tw/2013.6\(4\).414](https://doi.org/10.6135/ijprt.org.tw/2013.6(4).414)

- 1111 Masselink, G., and Pattiaratchi, C. B.: The effect of sea breeze on beach morphology, surf zone
1112 hydrodynamics and sediment resuspension, *Mar. Geol.*, 146, 115–135, 1998.
- 1113 Mather, J. H., and Voyles, J. W.: The Arm Climate Research Facility: A Review of Structure
1114 and Capabilities. *Bull. Amer. Meteor. Soc.*, 94, 377–392,
1115 <https://doi.org/10.1175/BAMS-D-11-00218.1>, 2013.
- 1116 Miller, S. T. K., Keim, B. D., Talbot, R. W., & Mao, H.: Sea breeze: Structure, forecasting,
1117 and impacts. *Reviews of Geophysics*, 41(3). <https://doi.org/10.1029/2003RG000124>,
1118 2003.
- 1119 Minguillón, M. C., Ripoll, A., Pérez, N., Prévôt, A. S. H., Canonaco, F., Querol, X., and
1120 Alastuey, A.: Chemical characterization of submicron regional background aerosols in
1121 the western Mediterranean using an Aerosol Chemical Speciation Monitor, *Atmos.*
1122 *Chem. Phys.*, 15, 6379–6391, <https://doi.org/10.5194/acp-15-6379-2015>, 2015.
- 1123 Mlawer, E. J., Taubman, S. J., Brown, P. D., Iacono, M., & Clough, S. A.: Radiative transfer
1124 for inhomogeneous atmospheres: RRTM, a validated correlated-k model for the
1125 longwave. *Journal of Geophysical Research*, 102(D14), 16663–16682.
1126 <https://doi.org/10.1029/97JD00237>, 1997.
- 1127 Monin, A. S., & Obukhov, A. M.: Basic laws of turbulent mixing in the surface layer of the
1128 atmosphere. *Contributions of the Geophysical Institute of the Slovak Academy of*
1129 *Science, USSR*, 151, 163–187, 1954.
- 1130 Moorthy, K. K., Murthy, B. V. K., and Nair, P. R.: Sea-breeze front effects on boundary layer
1131 aerosols at a tropical station, *J. Appl. Meteorol.*, 32, 1196–1205. 1993.
- 1132 Moorthy, K. K., Pillai, P. S., & Suresh Babu, S.: Influence of changes in the prevailing synoptic
1133 conditions on the response of aerosol characteristics to land-and sea-breeze circulations
1134 at a coastal station. In *Boundary-Layer Meteorology (Vol. 108)*, 2003.
- 1135 Morrison, H., Curry, J. A., and Khvorostyanov, V. I.: A new double-moment microphysics
1136 parameterization for application in cloud and climate models. Part I: Description.
1137 *Journal of the Atmospheric Sciences*, 62(6), 1665–1677.
1138 <https://doi.org/10.1175/jas3446.1>, 2005.

- 1139 Papanastasiou, D. K., Melas, D., Bartzanas, T., & Kittas, C.: Temperature, comfort and
1140 pollution levels during heat waves and the role of sea breeze. *International Journal of*
1141 *Biometeorology*, 54(3), 307–317. <https://doi.org/10.1007/s00484-009-0281-9>, 2010.
- 1142 Parajuli, S. P., Stenchikov, G. L., Ukhov, A., Mostamandi, S., Kucera, P. A., Axisa, D.,
1143 Gustafson, W. I., & Zhu, Y.: Effect of dust on rainfall over the Red Sea coast based on
1144 WRF-Chem model simulations. *Atmospheric Chemistry and Physics*, 22(13), 8659–
1145 8682. <https://doi.org/10.5194/acp-22-8659-2022>, 2022.
- 1146 Parajuli, S., Stenchikov, G. G., Ukhov, A., Shevchenko, I., Dubovik, O., & Lopatin, A.:
1147 Aerosol vertical distribution and interactions with land/sea breezes over the eastern
1148 coast of the Red Sea from lidar data and high-resolution WRF-Chem simulations.
1149 *Atmospheric Chemistry and Physics*, 20(24), 16089–16116.
1150 <https://doi.org/10.5194/acp-20-16089-2020>, 2020.
- 1151 Park, J. M., van den Heever, S. C., Igel, A. L., Grant, L. D., Johnson, J. S., Saleeby, S. M.,
1152 Miller, S. D., & Reid, J. S. (2020). Environmental Controls on Tropical Sea Breeze
1153 Convection and Resulting Aerosol Redistribution. *Journal of Geophysical Research:*
1154 *Atmospheres*, 125(6). <https://doi.org/10.1029/2019JD031699>, 2020.
- 1155 Park, M. J., and van den Heever, S. C.: Weakening of tropical sea breeze convective systems
1156 through interactions of aerosol, radiation, and soil moisture. *Atmospheric Chemistry*
1157 *and Physics*, 22(16), 10527–10549. <https://doi.org/10.5194/acp-22-10527-2022>, 2022.
- 1158 Parrish, D. D., Allen, D. T., Bates, T. S., Estes, M., Fehsenfeld, F. C., Feingold, G., Ferrare,
1159 R., Hardesty, R. M., Meagher, J. F., Nielsen-Gammon, J. W., Pierce, R. B., Ryerson,
1160 T. B., Seinfeld, J. H., & Williams, E. J.: Overview of the second texas air quality study
1161 (TexAQS II) and the Gulf of Mexico atmospheric composition and climate study
1162 (GoMACCS). *Journal of Geophysical Research Atmospheres*, 114(13).
1163 <https://doi.org/10.1029/2009JD011842>, 2009.
- 1164 Partanen, A. I., Landry, J. S., and Matthews, H. D.: Climate and health implications of future
1165 aerosol emission scenarios. *Environmental Research Letters*, 13(2).
1166 <https://doi.org/10.1088/1748-9326/aaa511>, 2018.
- 1167 Perry, K. D., Cahill, T. A., Eldred, R. A., Dutcher, D. D., and Gill, T. E.: Long-range transport
1168 of North African dust to the eastern United States. *Journal of Geophysical Research*
1169 *Atmospheres*, 102(10), 11225–11238. <https://doi.org/10.1029/97jd00260>, 1997.

- 1170 Pinto, J. P., Dibb, J., Lee, B. H., Rappenglück, B., Wood, E. C., Levy, M., Zhang, R. Y., Lefer,
1171 B., Ren, X. R., Stutz, J., Tsai, C., Ackermann, L., Golovko, J., Herndon, S. C., Oakes,
1172 M., Meng, Q. Y., Munger, J. W., Zahniser, M., & Zheng, J.: Intercomparison of field
1173 measurements of nitrous acid (HONO) during the SHARP campaign. *Journal of*
1174 *Geophysical Research*, 119(9), 5583–5601. <https://doi.org/10.1002/2013JD020287>,
1175 2014.
- 1176 Plant, R. S., & Keith, G. J.: Occurrence of Kelvin-Helmholtz billows in sea-breeze circulations.
1177 *Boundary-Layer Meteorology*, 122(1), 1–15. [https://doi.org/10.1007/s10546-006-](https://doi.org/10.1007/s10546-006-9089-x)
1178 9089-x, 2007.
- 1179 Qi, L., Vogel, A. L., Esmaeilirad, S., Cao, L., Zheng, J., Jaffrezo, J. L., Fermo, P., Kasper-
1180 Giebl, A., Daellenbach, K. R., Chen, M., Ge, X., Baltensperger, U., Prévôt, A. S. H., &
1181 Slowik, J. G.: A 1-year characterization of organic aerosol composition and sources
1182 using an extractive electrospray ionization time-of-flight mass spectrometer (EESI-
1183 TOF). *Atmospheric Chemistry and Physics*, 20(13), 7875–7893.
1184 <https://doi.org/10.5194/acp-20-7875-2020>, 2020.
- 1185 Ramanathan, V., Crutzen, P. J., Kiehl, J. T., & Rosenfeld, D.: Aerosols, Climate, and the
1186 Hydrological Cycle. *Science*, 294, 5549, DOI: 10.1126/science.1064034, 2001.
- 1187 Rao, P. A., & Fuelberg, H. E.: An Investigation of Convection behind the Cape Canaveral Sea-
1188 Breeze Front, 2000.
- 1189 Rapp, A. D., Brooks, S. D., Nowotarski, C. J., Sharma, M., Thompson, S. A., Chen, B., et al.
1190 (2024). TAMU TRACER: Targeted mobile measurements to isolate the impacts of
1191 aerosols and meteorology on deep convection. *Bulletin of the American Meteorological*
1192 *Society*, 105(9), E1685–E1702. <https://doi.org/10.1175/BAMS-D-23-0218.1>
- 1193 Rodier, Q., Masson, V., Couvreux, F., & Paci, A. (2017). Evaluation of a buoyancy and shear
1194 based mixing length for a turbulence scheme. *Frontiers in Earth Science*, 5.
1195 <https://doi.org/10.3389/feart.2017.00065>
- 1196 Rosenfeld, D., et al.: Flood or drought: How do aerosols affect precipitation? *Science*, 321,
1197 1309–1313, 2008.
- 1198 Ryerson, T. B., Trainer, M., Angevine, W. M., Brock, C. A., Dissly, R. W., Fehsenfeld, F. C.,
1199 Frost, G. J., Goldan, P. D., Holloway, J. S., Hübler, G., Jakoubek, R. O., Kuster, W. C.,

1200 Neuman, J. A., Nicks, D. K., Parrish, D. D., Roberts, J. M., Sueper, D. T., Atlas, E. L.,
1201 Donnelly, S. G., et al.: Effect of petrochemical industrial emissions of reactive alkenes
1202 and NO_x on tropospheric ozone formation in Houston, Texas. *Journal of Geophysical*
1203 *Research: Atmospheres*, 108(8). <https://doi.org/10.1029/2002jd003070>, 2003.

1204 Schell, B., Ackerman, I. J., Hass, H., Binkowski, F. S., & Ebel, A.: Modelling the formation
1205 of secondary organic aerosol within a comprehensive air quality model system. *Journal*
1206 *of Geophysical Research*, 106(D22), 28275–28293.
1207 <https://doi.org/10.1029/2001JD000384>, 2001.

1208 Seinfeld, J.H.; Pandis, S.N. *Atmospheric Chemistry and Physics: From Air Pollution to*
1209 *Climate Change*, 2nd ed.; Wiley: Hoboken, NJ, USA, 2006.

1210 Sharma, M., Rapp, A. D., Nowotarski, C. J., & Brooks, S. D. (2024). Observed Variability in
1211 Convective Cell Characteristics and Near-Storm Environments across the Sea- and
1212 Bay-Breeze Fronts in Southeast Texas. *Monthly Weather Review*, 152(11), 2419–2441.
1213 <https://doi.org/10.1175/MWR-D-23-0243.1>

1214 Shrestha, S., Zhou, S., Mehra, M., Guagenti, M., Yoon, S., Alvarez, S. L., Guo, F., Chao, C.
1215 Y., Flynn, J. H., Wang, Y., Griffin, R. J., Usenko, S., & Sheesley, R. J.: Evaluation of
1216 aerosol- and gas-phase tracers for identification of transported biomass burning
1217 emissions in an industrially influenced location in Texas, USA. *Atmospheric Chemistry*
1218 *and Physics*, 23(19), 10845–10867. <https://doi.org/10.5194/acp-23-10845-2023>, 2023.

1219 Shrivastava, M., Zhang, J., Zaveri, R. A., Zhao, B., Pierce, J. R., O'Donnell, S. E., et al.:
1220 Anthropogenic extremely low volatility organics (ELVOCs) govern the growth of
1221 molecular clusters over the Southern Great Plains during the springtime. *Journal of*
1222 *Geophysical Research: Atmospheres*, 129, e2024JD041212,
1223 <https://doi.org/10.1029/2024JD041212>, 2024.

1224 Simpson, J. E.: *Sea Breeze and Local Wind*, 234 pp., Cambridge Univ. Press, New York, 1994.

1225 Singh, A. and Kuang, C.: *Scanning Mobility Particle Sizer (SMPS) Instrument Handbook*. U.S.
1226 Department of Energy, Atmospheric Radiation Measurement user facility, Richland,
1227 Washington. DOE/SC-ARM-TR-147, 2024.

- 1228 Skamarock, W. C., Klemp, J. B., Dudhia, J., Gill, D. O., Barker, D., Wang, W., Powers, J. G.:
1229 A description of the Advanced Research WRF version 3. NCAR Tech. Note
1230 NCAR/TN-475+STR, 113 pp., doi:10.5065/D68S4MVH, 2008.
- 1231 Song, S. K., Choi, Y. N., Choi, Y., Flynn, J., & Sadeghi, B.: Characteristics of aerosol chemical
1232 components and their impacts on direct radiative forcing at urban and suburban
1233 locations in Southeast Texas. *Atmospheric Environment*, 246.
1234 <https://doi.org/10.1016/j.atmosenv.2020.118151>, 2021. Maria, V. D., Rahman, M.,
1235 Collins, P., Dondi, G., & Sangiorgi, C. (2013). Urban Heat Island Effect: Thermal
1236 Response from Different Types of Exposed Paved Surfaces. *International Journal of*
1237 *Pavement Research and Technology*, 6(4), 414-422.
1238 [https://doi.org/10.6135/ijprt.org.tw/2013.6\(4\).414](https://doi.org/10.6135/ijprt.org.tw/2013.6(4).414)
- 1239 Soni, M., Verma, S., Mishra, M. K., Mall, R. K., and Payra, S.: Estimation of particulate matter
1240 pollution using WRF-Chem during dust storm event over India. *Urban Climate*, 44.
1241 <https://doi.org/10.1016/j.uclim.2022.101202>, 2022.
- 1242 Stockwell, W. R., Middleton, P., Chang, J. S., and Tang, X.: The second generation regional
1243 acid deposition model chemical mechanism for regional air quality modeling. *Journal*
1244 *of Geophysical Research*, 95(D10), 16343–16367.
1245 <https://doi.org/10.1029/JD095iD10p16343>, 1990.
- 1246 Subba, T., Zhang, Y., & Steiner, A. L.: Simulating the transport and rupture of pollen in the
1247 atmosphere. *Journal of Advances in Modeling Earth Systems*, 15, e2022MS003329.
1248 <https://doi.org/10.1029/2022MS003329>, 2023.
- 1249 Subramanian, A., Nagarajan, A. M., Vinod, S., Chakraborty, S., Sivagami, K., Theodore, T.,
1250 Sathyanarayanan, S. S., Tamizhdurai, P., & Mangesh, V. L. (2023). Long-term impacts
1251 of climate change on coastal and transitional eco-systems in India: an overview of its
1252 current status, future projections, solutions, and policies. In *RSC Advances* (Vol. 13,
1253 Issue 18, pp. 12204–12228). Royal Society of Chemistry.
1254 <https://doi.org/10.1039/d2ra07448f>
- 1255 Talbot, C., Augustin, P., Leroy, C., Willart, V., Delbarre, H., Khomenko, G.: Impact of a sea
1256 breeze on the boundary-layer dynamics and the atmospheric stratification in a coastal
1257 area of the North Sea. *BoundaryLayer Meteorology*, 125, 133–154, 2007.

- 1258 Thompson, S. A., Chen, B., Matthews, B.H., Li, R., Nowotarski, C. J., Rapp, A. D., & Brooks,
1259 S. D. (2025). Characterizing Greater Houston's aerosol by air mass during TRACER.
1260 *Journal of Geophysical Research: Atmospheres*, 130, e2025JD043353.
1261 <https://doi.org/10.1029/2025JD043353>.
- 1262 Tuccella, P., Curci, G., Visconti, G., Bessagnet, B., Menut, L., & Park, R. J.: Modeling of gas
1263 and aerosol with WRF/Chem over Europe: Evaluation and sensitivity study. *Journal of*
1264 *Geophysical Research Atmospheres*, 117(3). <https://doi.org/10.1029/2011JD016302>,
1265 2012.
- 1266 Twomey, S.: Pollution and the planetary albedo. *Atmos. Environ.*, 8, 1251–1256, 1974.
- 1267 Uin, J., Aiken, A. C., Dubey, M. K., Kuang, C., Pekour, M., Salwen, C., Sedlacek, A. J.,
1268 Senum, G., Smith, S., Wang, J., Watson, T. B., & Springston, S. R.: Atmospheric
1269 radiation measurement (ARM) aerosol observing systems (AOS) for surface-based in
1270 situ atmospheric aerosol and trace gas measurements. *Journal of Atmospheric and*
1271 *Oceanic Technology*, 36(12), 2429–2447. [https://doi.org/10.1175/JTECH-D-19-](https://doi.org/10.1175/JTECH-D-19-0077.1)
1272 [0077.1](https://doi.org/10.1175/JTECH-D-19-0077.1), 2019.
- 1273 Verma, S., Boucher, O., Venkataraman, C., Reddy, M. S., Müller, D., Chazette, P., &
1274 Crouzille, B.: Aerosol lofting from sea breeze during the Indian Ocean Experiment.
1275 *Journal of Geophysical Research*, 111, 07208. <https://doi.org/10.1029/2005JD005953> ,
1276 2006.
- 1277 Viner, B., Noble, S., Qian, J. H., Werth, D., Gayes, P., Pietrafesa, L., and Bao, S.: Frequency
1278 and characteristics of inland advecting sea breezes in the Southeast United States.
1279 *Atmosphere*, 12(8). <https://doi.org/10.3390/atmos12080950>, 2021.
- 1280 Wang, B., Geddes, J. A., Adams, T. J., Lind, E. S., McDonald, B. C., He, J., Harkins, C., Li,
1281 D., and Pfister, G. G.: Implications of Sea Breezes on Air Quality Monitoring in a
1282 Coastal Urban Environment: Evidence From High Resolution Modeling of NO₂ and
1283 O₃. *Journal of Geophysical Research: Atmospheres*, 128(11).
1284 <https://doi.org/10.1029/2022jd037860>, 2023.
- 1285 Wang, D., Jensen, M. P., Taylor, D., Kowalski, G., Hogan, M., Wittemann, B. M.,
1286 Rakotoarivony, A., Giangrande, S. E., & Park, J. M.: Linking Synoptic Patterns to
1287 Cloud Properties and Local Circulations Over Southeastern Texas. *Journal of*

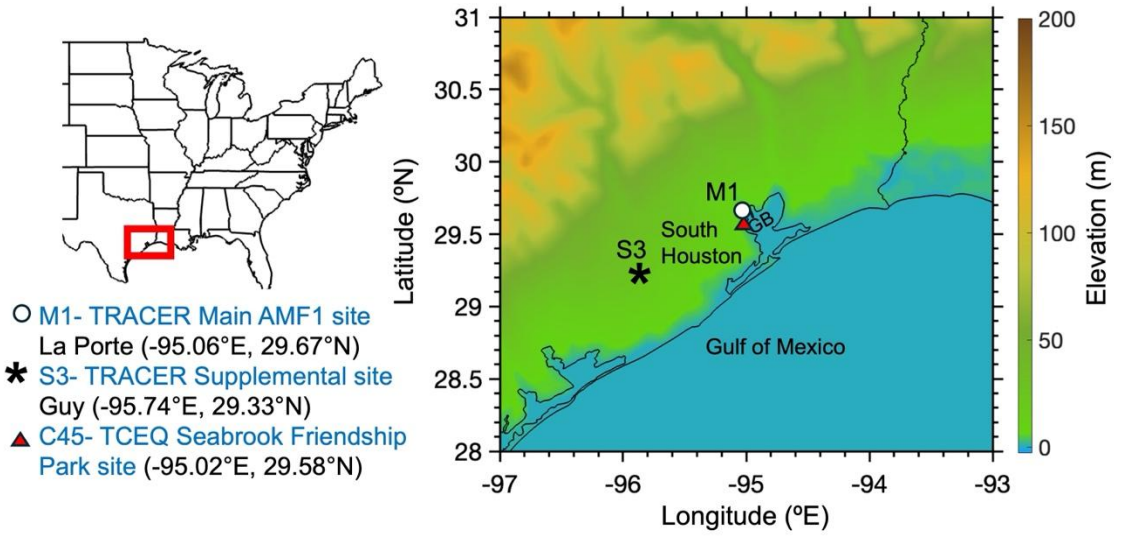
- 1288 Geophysical Research: Atmospheres, 127(5). <https://doi.org/10.1029/2021JD035920>,
1289 2022.
- 1290 Wang, D., Melvin, E. C., Smith, N., Jensen, M. P., Gupta, S., Abdullah-Smoot, A., Pszeniczny,
1291 N., & Hahn, T.: TRACER Perspectives on Gulf-Breeze and Bay-Breeze Circulations
1292 and Coastal Convection. *Monthly Weather Review*, 152(10), 2207–2228.
1293 <https://doi.org/10.1175/MWR-D-23-0292.1>, 2024.
- 1294 Wang, K., Zhang, Y., Yahya, K.: Decadal application of WRF/Chem over the continental U.S.:
1295 Simulation design, sensitivity simulations, and climatological model evaluation.
1296 *Atmospheric Environment*, 253, 118331,
1297 <https://doi.org/10.1016/j.atmosenv.2021.118331>, 2021.
- 1298 Wang, S. C., Wang, Y., Estes, M., Lei, R., Talbot, R., Zhu, L., & Hou, P.: Transport of Central
1299 American Fire Emissions to the U.S. Gulf Coast: Climatological Pathways and Impacts
1300 on Ozone and PM_{2.5}. *Journal of Geophysical Research: Atmospheres*, 123(15), 8344–
1301 8361. <https://doi.org/10.1029/2018JD028684>, 2018.
- 1302 Watson, TB.: Aerosol Chemical Speciation Monitor (ACSM) Instrument Handbook. U.S.
1303 Department of Energy, Atmospheric Radiation Measurement user facility, Richland,
1304 Washington.DOE/SC-ARM-TR-196, 2024.
- 1305 Wert, B. P., Trainer, M., Fried, A., Ryerson, T. B., Henry, B., Potter, W., Angevine, W. M.,
1306 Atlas, E., Donnelly, S. G., Fehsenfeld, F. C., Frost, G. J., Goldan, P. D., Hansel, A.,
1307 Holloway, J. S., Hubler, G., Kuster, W. C., Nicks, D. K., Neuman, J. A., Parrish, D. D.,
1308 ... Wisthaler, A.: Signatures of terminal alkene oxidation in airborne formaldehyde
1309 measurements during TexAQS 2000. *Journal of Geophysical Research D:*
1310 *Atmospheres*, 108(3). <https://doi.org/10.1029/2002jd002502>, 2003.
- 1311 Westenbarger, D. A., & Morris, G. A.: Identifying biomass burning impacts on air quality in
1312 Southeast Texas 26–29 August 2011 using satellites, models and surface data.
1313 <https://doi.org/10.5194/acp-2017-1234>, 2018.
- 1314 Yoon, S., Ortiz, S. M., Clark, A. E., Barrett, T. E., Usenko, S., Duvall, R. M., Ruiz, L. H.,
1315 Bean, J. K., Faxon, C. B., Flynn, J. H., Lefer, B. L., Leong, Y. J., Griffin, R. J., &
1316 Sheesley, R. J.: Apportioned primary and secondary organic aerosol during pollution
1317 events of DISCOVER-AQ Houston. *Atmospheric Environment*, 244.
1318 <https://doi.org/10.1016/j.atmosenv.2020.117954>, 2021.

1319

1320

1321

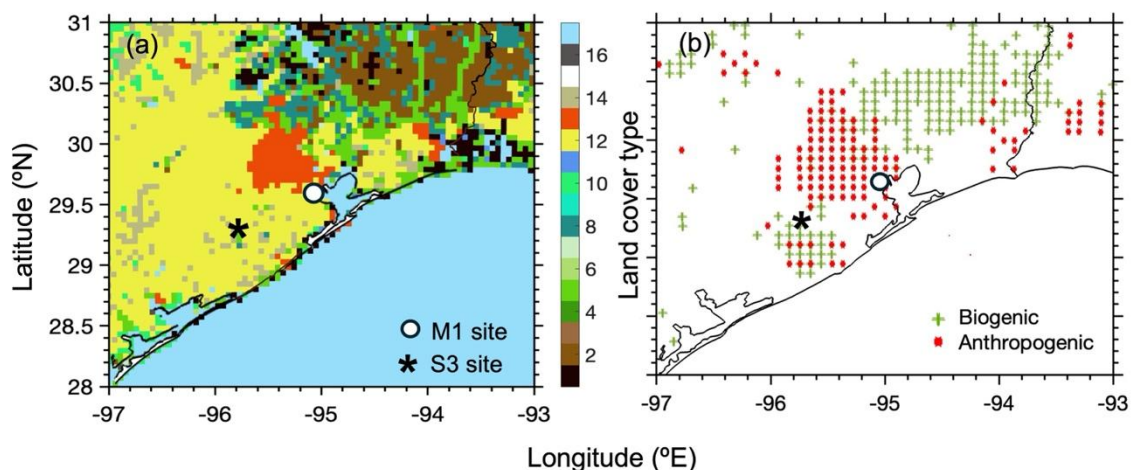
1322
1323
1324



1325
1326
1327
1328
1329
1330
1331
1332
1333
1334
1335
1336
1337
1338
1339

Figure 1. Map showing the TRACER field campaign main site (M1) and supplemental site (S3), and the TCEQ Seabrook Friendship Park site (C45). Terrain elevation is shown in color. Here, “GB” corresponds to the Galveston Bay.

1340
1341
1342
1343



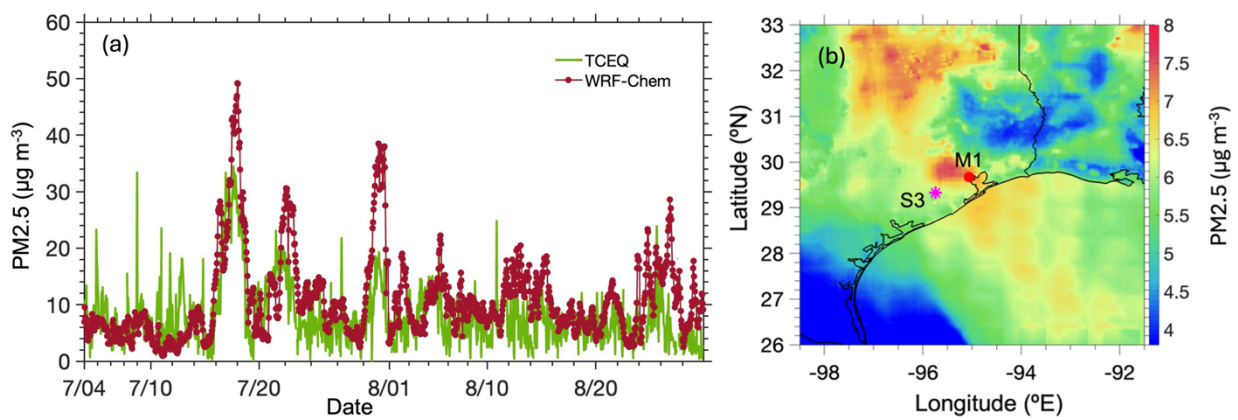
1344

1345 **Figure 2.** Weather Research and Forecasting model coupled with Chemistry (WRF-Chem)
1346 simulation domain with (a) primary land cover types comprising of (1) Evergreen Needleleaf
1347 Forest, (2) Evergreen Broadleaf Forest, (3) Deciduous Needleleaf Forest, (4) Deciduous
1348 Broadleaf Forest, (5) Mixed Forest, (6) Closed Shrubland, (7) Open Shrubland, (8) Woody
1349 Savanna, (9) Savanna, (10) Grassland, (11) Permanent Wetlands, (12) Cropland, (13) Urban
1350 and Build-up, (14) Cropland/Natural Mosaic, (15) Snow and Ice, (16) Barren or Sparsely
1351 Vegetated, and (17) Water; (b) Anthropogenic (red dots) and biogenic (green dots) aerosol
1352 emission source points obtained using the National Emissions Inventory (NEI) data and Model
1353 of Emissions of Gases and Aerosols from Nature (MEGAN) modeling system, respectively.

1354
1355
1356
1357
1358
1359
1360

1361

1362



1363

1364 **Figure 3.** (a) Comparison of daily averaged PM_{2.5} observed (green) at the TCEQ site, and
1365 WRF-Chem simulated (red) at the M1 site. (b) Spatial distribution of WRF-Chem simulated
1366 August 2022 mean PM_{2.5} (filled contours).

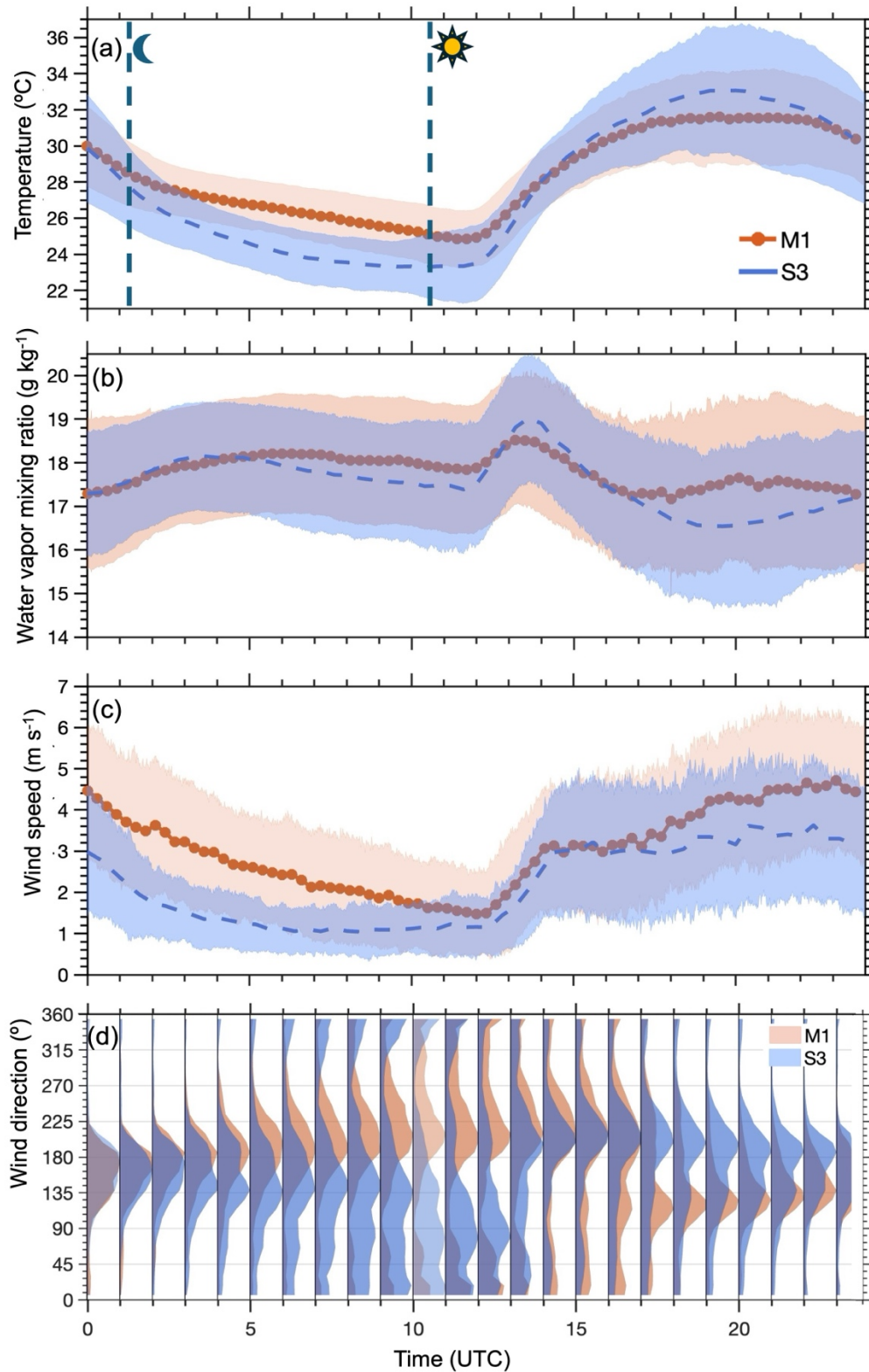
1367

1368

1369

1370

1371



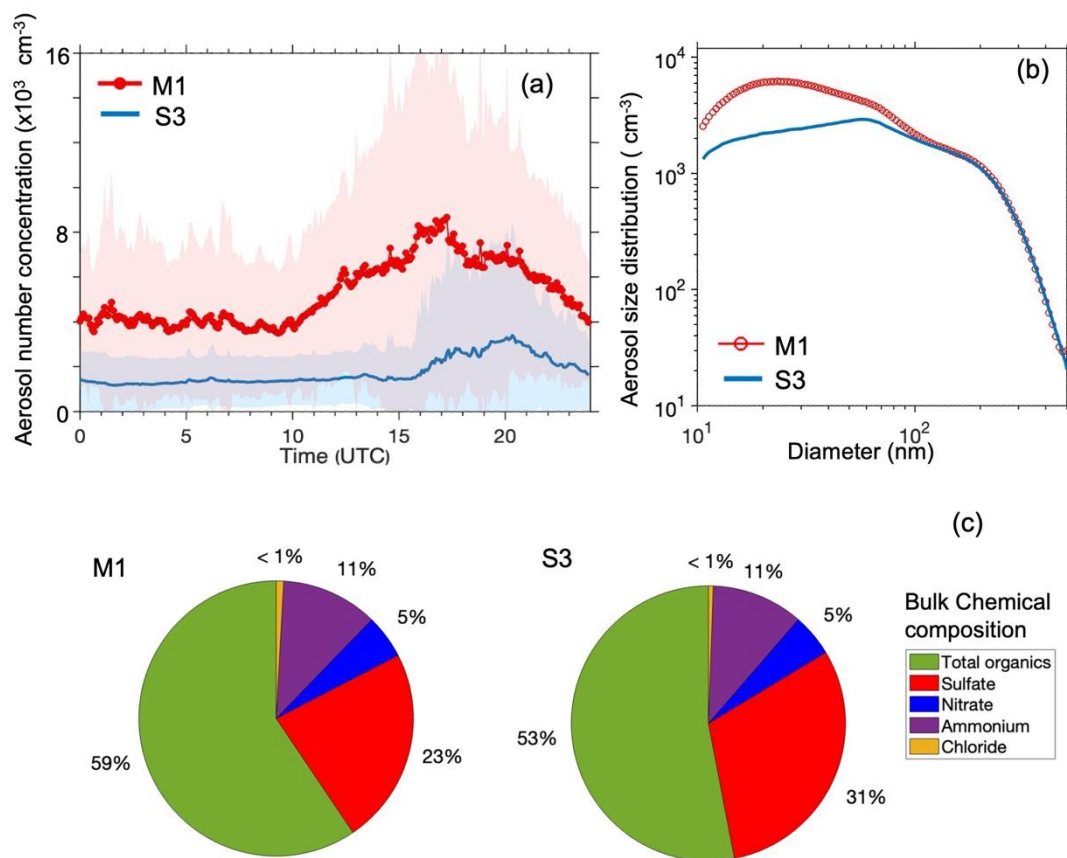
1372

1373 **Figure 4.** Diurnal variation of meteorological variables (a) Temperature at 2 m, (b) water vapor
 1374 mixing ratio (w) (c) wind speed at 10 m, and (d) wind direction waterfall diagram at 10 m
 1375 measured at M1 (in orange) and S3 (in blue) sites averaged during IOP. The shaded color
 1376 represents the standard deviation from the mean.

1377

1378

1379



1380

1381 **Figure 5.** Measured (a) diurnal distribution of aerosol number concentration, (b) aerosol size
1382 distribution, and (c) percentage contribution of bulk chemical composition at M1 and S3 sites
1383 averaged from June to September 2022.

1384

1385

1386

1387

1388

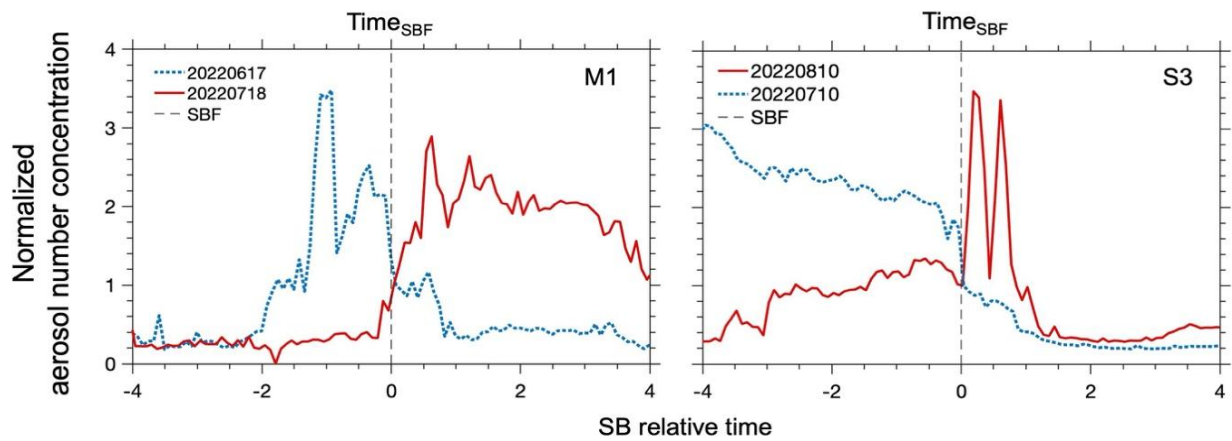
1389

1390

1391

1392

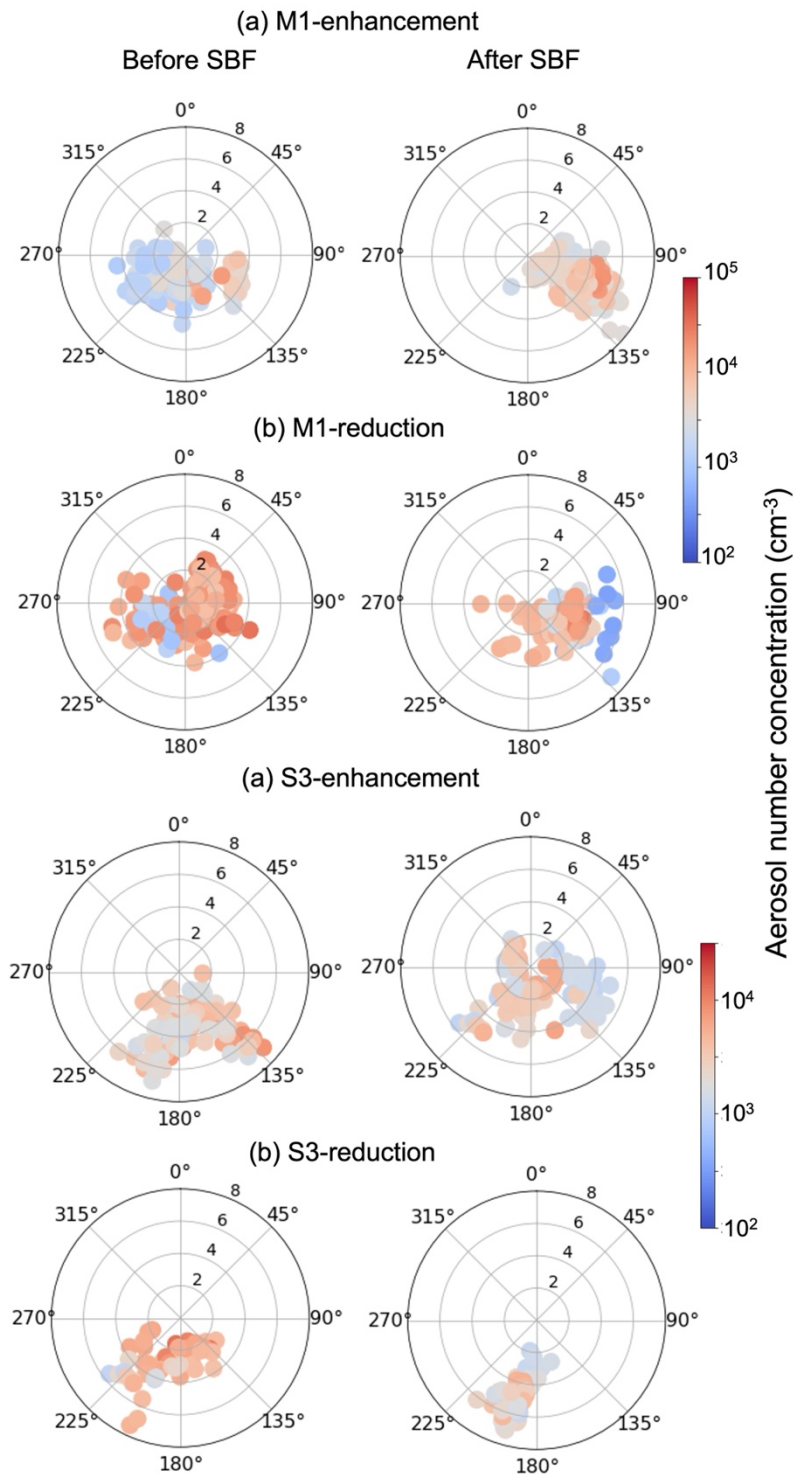
1393



1394

1395 **Figure 6.** Time series of the normalized aerosol number concentration, with the time centered
1396 at the time of the passing of the SBF ($T_{\text{SBF}}=0$) at the M1 site (1st column) and the S3 site (2nd
1397 column) during the individual SB event days.

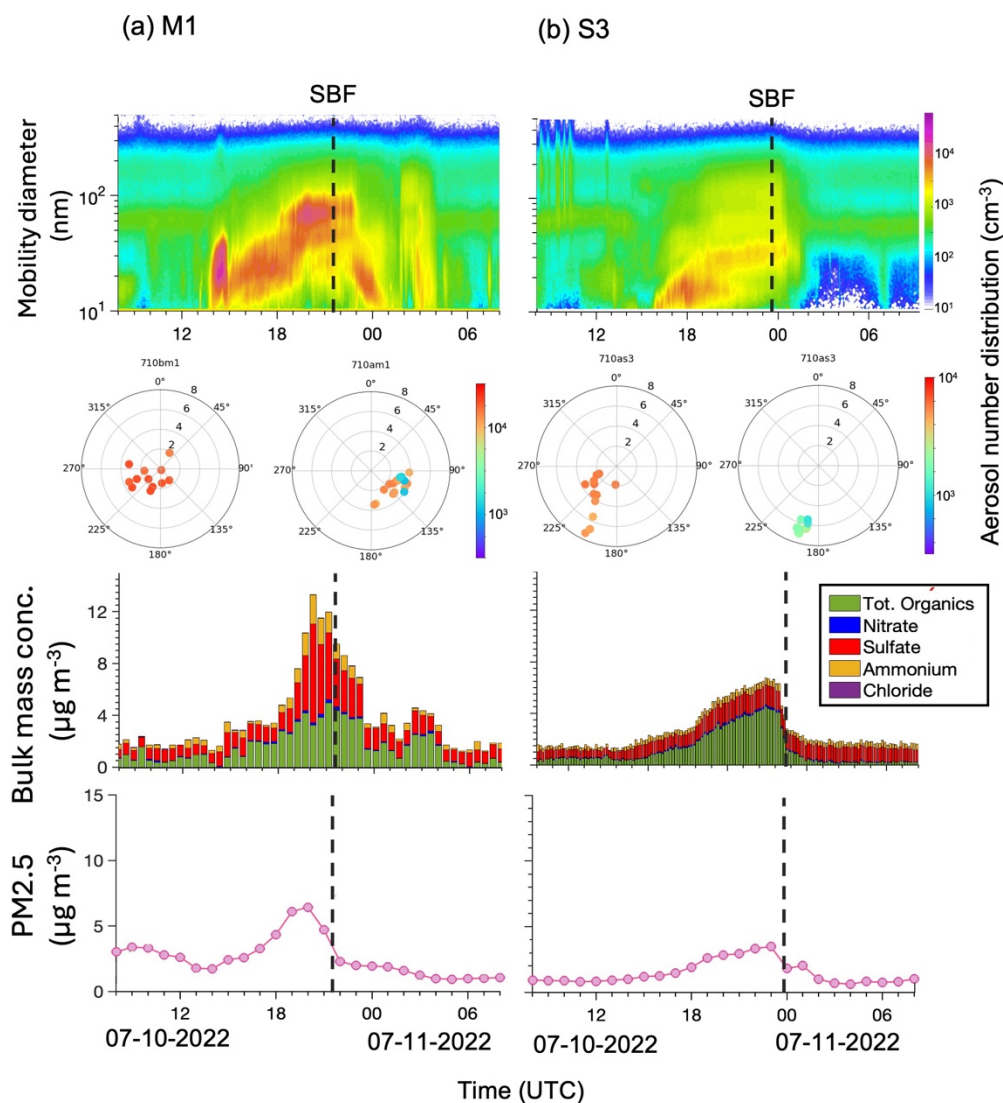
1398



1399

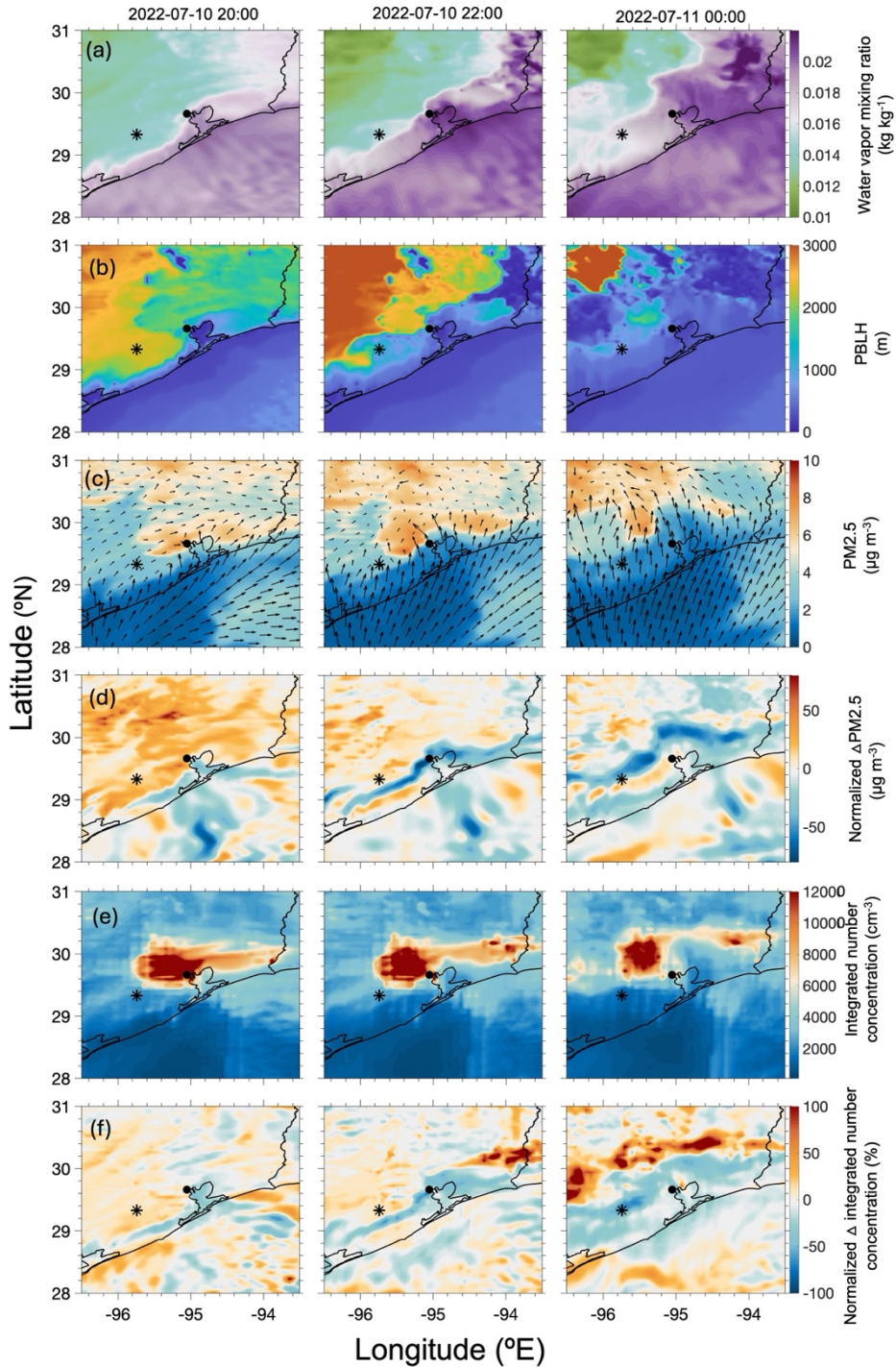
1400 **Figure 7.** Open-air polar plots for aerosol number concentration before and after the passing
 1401 of the SBF ($\Delta T = T_{\text{SBF}\pm 1}$) during (a) enhancement and (b) reduction events at M1 and S3 sites.
 1402 The wind speed (in m s^{-1}) grid lines are presented with black circles; the color scales represent
 1403 the concentrations observed with each wind speed and direction combinations.

1404
1405
1406
1407



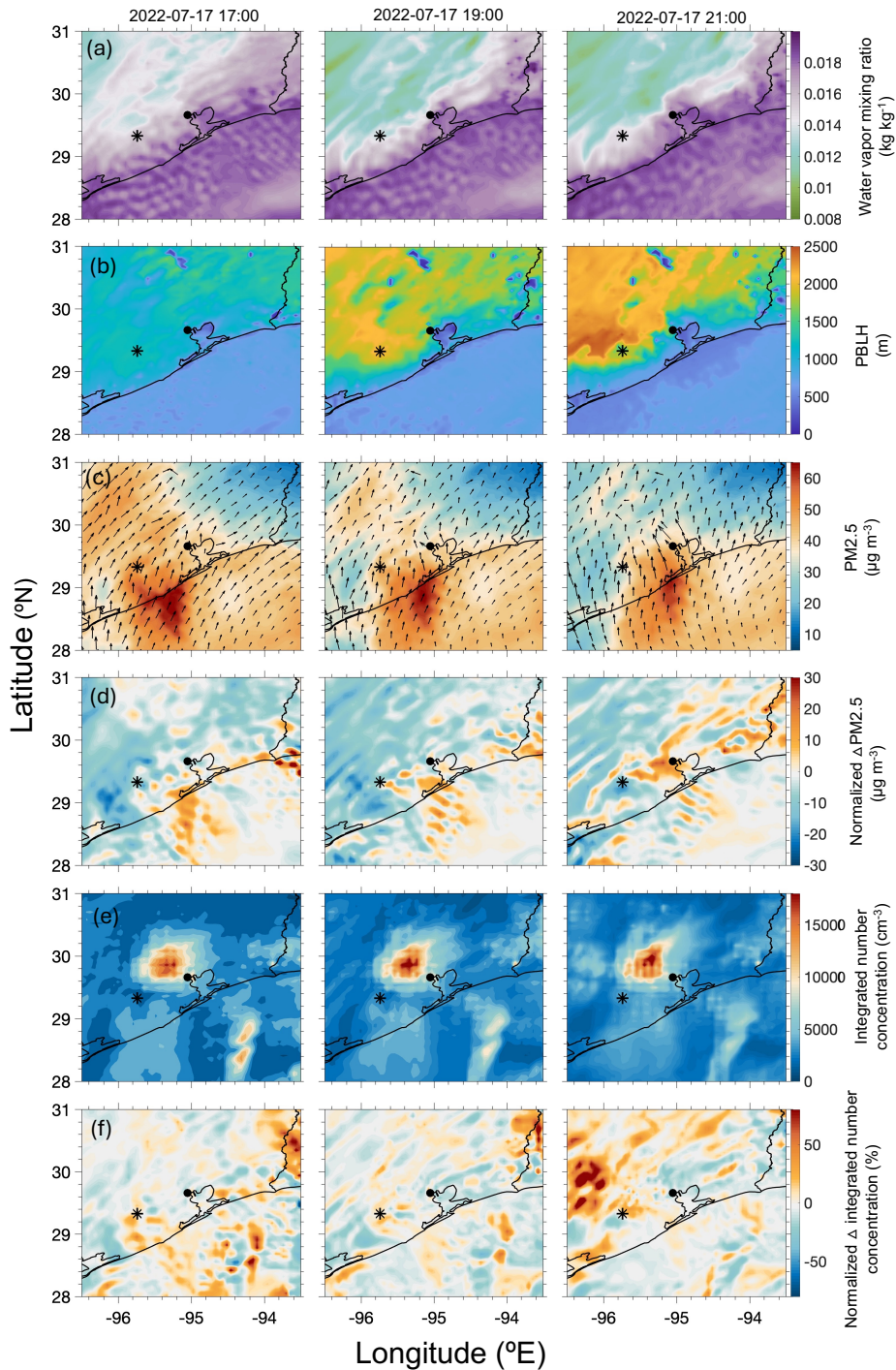
1408
1409
1410
1411
1412
1413

Figure 8. Time series of measured aerosol size distribution (1st row), measured bulk chemical composition (3rd row), and modeled PM_{2.5} mass concentration (4th row) at (a) M1 and (b) S3 on 10 July 2022. Polar plot showing the measured integrated aerosol number concentration during one hour before and after the passing of the SBF (2nd row). The black dashed line represents the time of the passing of the SBF (T_{SBF}) at the respective sites.



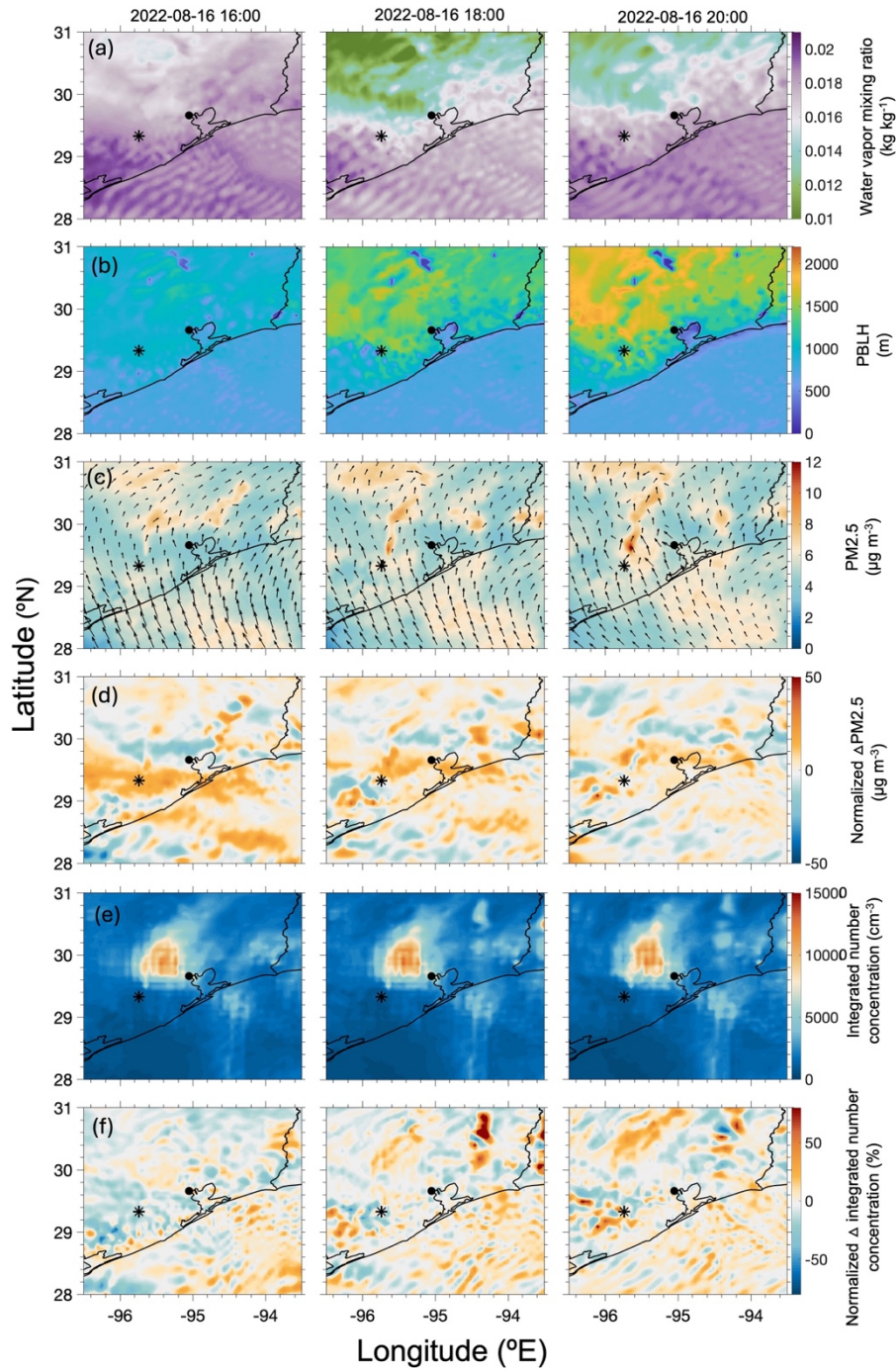
1414

1415 **Figure 9.** Modeled surface distribution of (a) water vapor mixing ratio (w), (b) PBLH, (c)
 1416 $PM_{2.5}$, and wind vector (black arrows, at the surface), and (e) integrated aerosol number
 1417 concentration (nucleation + accumulation mode) at three-time steps: 20:00 and 22:00 UTC on
 1418 10 July, and 00:00 UTC on 11 July. Sub-panels (d) and (f) show the normalized changes, where
 1419 Δ is the change from the previous time step. The filled-circle marker in the panels represent the
 1420 M1 site, while the star represents the S3 site.



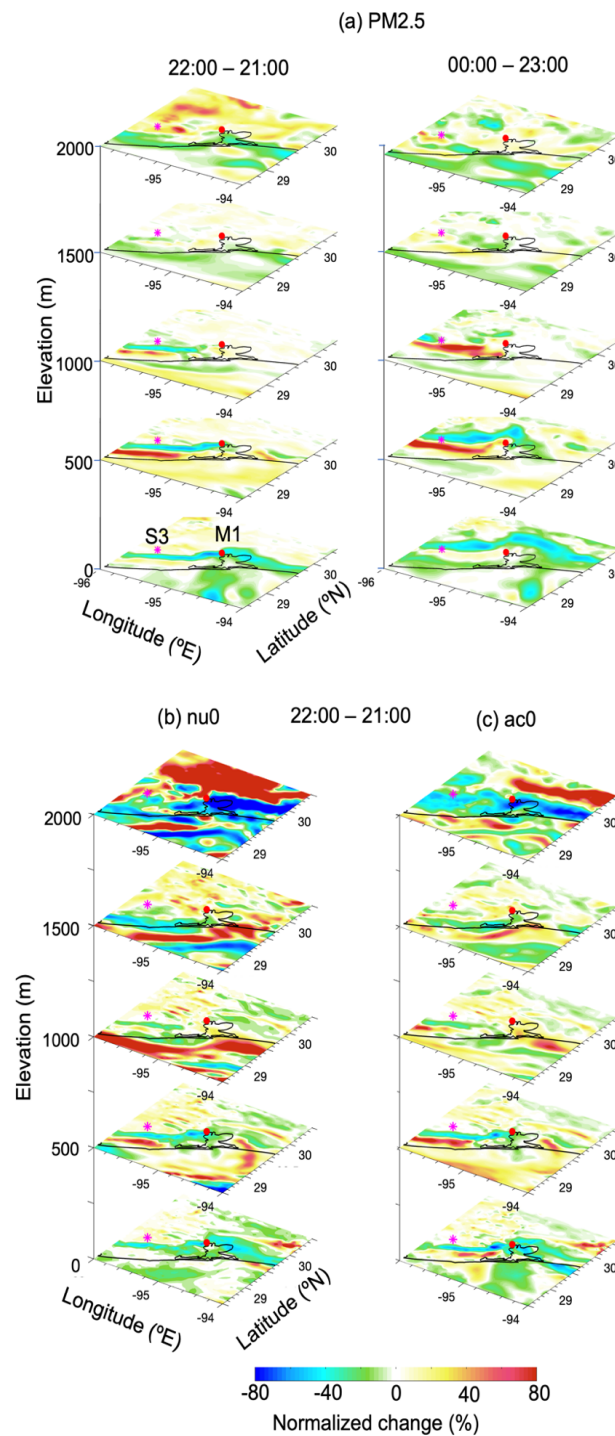
1421

1422 **Figure 10.** Modeled surface distribution of (a) water vapor mixing ratio (w), (b) PBLH, (c)
 1423 $PM_{2.5}$, and wind vector (black arrows, at the surface), and (e) integrated aerosol number
 1424 concentration (nucleation + accumulation mode) at three-time steps: 17:00, 19:00 and 21:00
 1425 UTC on 17 July. Sub-panels (d) and (f) show the normalized changes, where Δ is the change
 1426 from the previous time step. The filled-circle marker in the panels represent the M1 site, while
 1427 the star represents the S3 site.



1428

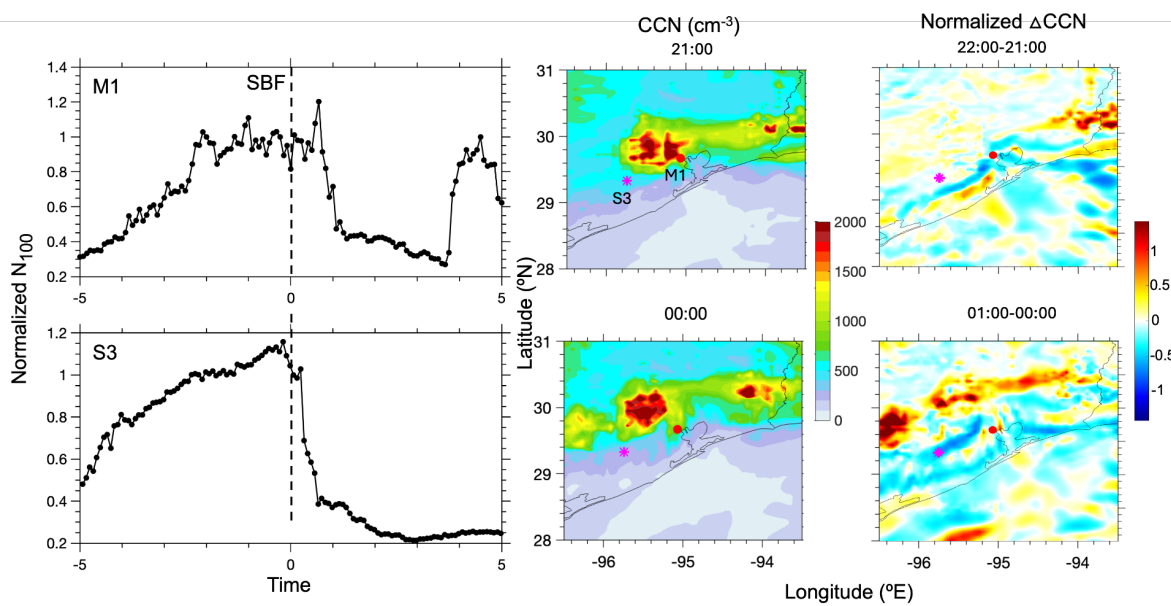
1429 **Figure 11.** Modeled surface distribution of (a) water vapor mixing ratio (w), (b) PBLH, (c)
 1430 $PM_{2.5}$, and wind vector (black arrows, at the surface), and (e) integrated aerosol number
 1431 concentration (nucleation + accumulation mode) at three-time steps: 16:00, 18:00 and 20:00
 1432 UTC on 16 August. Sub-panels (d) and (f) show the normalized changes, where Δ is the change
 1433 from the previous time step. The filled-circle marker in the panels represent the M1 site, while
 1434 the star represents the S3 site.



1436

1437 **Figure 12.** First row: the spatial distribution of normalized $\Delta\text{PM}_{2.5}$ at different elevations at
 1438 timesteps (a) 21:00 and 22:00 UTC on 10 July, and 23:00 UTC on 10 July and 00:00 UTC on
 1439 11 July. Second row: the spatial distribution of normalized (b) Δ nucleation mode (nu0) and (c)
 1440 Δ accumulation mode (ac0) aerosol number concentration at timesteps 21:00 and 22:00 UTC
 1441 on 10 July.

1442
1443
1444
1445
1446
1447
1448



1449
1450
1451
1452
1453
1454
1455
1456
1457
1458
1459

Figure 13. Time series of the normalized measured N_{100} along the time of the SBF's passing through the M1 site (first row) and the S3 site (second row) on 10 July 2022 (1st column). Spatial distribution of the modeled hourly averaged (2nd column) and normalized ΔCCN (3rd column).

1460

1461 **Table 1:** Summary of SBC influence on aerosol number concentration at the M1 and S3 sites.
1462 Events are classified into enhancement, reduction, and neutral categories.

1463

Site	Description	Combined	Enhancement	Reduction	Neutral
M1	Days (fraction of the total events %)	46 (total SB events)	13 (28 %)	16 (35 %)	17 (37 %)
	Concentration change (after - before) %	-23 (all enhancement + reduction events)	+55	-42	-11
		-7 (total number of events)			
S3	Days	30 (total SB events)	8 (27 %)	4 (13 %)	18 (60 %)
	Concentration change (after - before) %	+9 (all enhancement + reduction events)	+64	-45	-10
		+3 (total number of events)			

1464

1465

1466

1467

1468

1469

1470

1471

1472

1473

1475 **Table 2.** Model configuration

Simulation period	1 July - 30 August 2022
Domain	26 to 33 °N and -98 to -92 °E
Horizontal resolution (dx)	5 x 5 km
Vertical resolution	45 layers from 1000-50 mb
Meteorological initial and boundary conditions	North America mesoscale (NAM) forecast output at T221 (32-km) resolution, 28 vertical levels (Bauman, 2010)
Shortwave radiation	Goddard shortwave radiation scheme (Chou et al., 1998)
Longwave radiation	The rapid radiative transfer mode (RRTM) (Mlawer et al., 1997)
Land surface	Community National Center for Environmental Prediction (NCEP), Oregon State University, Air Force, and Hydrologic Research Lab-NWS Land Surface Model (NOAH) (Chen and Dudhia, 2001)
Surface Layer	Monin-Obukhov (Monin and Obukhov, 1954; Janjic, 2002)
PBL	Yonsei University Scheme (YSU) (Hong et al., 2006)
Cumulus	The Grell scheme (Grell and Devenyi 2002)
Microphysics	Morrison 2-moment scheme (Morrison, 2005)
Chemical mechanism	RACM Chemistry with MADE/VBS aerosols using KPP library along with the volatility basis set (VBS) used for Secondary Organic Aerosols (Stockwell et al., 1990; Ackerman et al., 1998; Schell et al., 2001)
Chemical initial and boundary conditions	MOZBC from the Model for Ozone and Related chemical Tracers (MOZART) model (Emmons et al., 2010)
Anthropogenic emissions	National Emissions Inventory (NEI), U.S. Environmental Protection Agency (EPA)
Biogenic emissions	The Model of Emissions of Gases and Aerosols from Nature version MEGAN v2.1 biogenic emissions (Guenther et al., 2012)